VERIFIED NOVEL DIFFUSION MRI SIGNATURES OF NEUROINFLAMMATION IN EXPERIMENTAL DIFFUSE TRAUMATIC BRAIN INJURY

By

Madeline M. Pressman

A Thesis Submitted to the Faculty of the

DEPARTMENT OF PSYCHIATRY

In Partial Fulfillment of the Requirements

For the Degree of

MASTER OF ARTS

In the Graduate College

THE UNIVERSITY OF ARIZONA

2025

THE UNIVERSITY OF ARIZONA
GRADUATE COLLEGE

As members of the Master's Committee, we certify that we have read the thesis prepared by: Madeline M. Pressman
titled: Verified Novel Diffusion MRI Signatures of Neuroinflammation in Experimental Diffuse Traumatic Brain Injury

and recommend that it be accepted as fulfilling the thesis requirement for the Master's Degree.

Jonathan Lifshitz — Date: Aug 21, 2025

L. Matthew LAw
L. Matthew LAw (Aug 21, 2025 12:43:08 PDT)
L. Matthew LAw — Date: Aug 21, 2025

Elizabeth Hutchinson — Date: Aug 21, 2025

Final approval and acceptance of this thesis is contingent upon the candidate's submission of the final copies of the thesis to the Graduate College.

I hereby certify that I have read this thesis prepared under my direction and recommend that it be accepted as fulfilling the Master's requirement.

Jonathan Lifshitz — Date: Aug 21, 2025
Thesis Committee Chair
Psychiatry - Phoenix

Table of Contents

Abstract

Diffuse traumatic brain injury (TBI) represents the most common form of brain injury, yet conventional magnetic resonance imaging (MRI) fails to detect neuroinflammatory pathophysiology without overt structural abnormalities. Diffusion MRI (dMRI) offers sensitivity to microscale pathophysiological changes, but imaging signatures, characteristic patterns on scans, require validation against histopathological markers. This study established radiologic-pathologic correspondence between dMRI signatures and histopathologic targets in experimental diffuse TBI. *Ex vivo* diffusion MRI was performed on adult Sprague Dawley rats (n = 4) 7 days post-injury using a 7T system with mean apparent propagator metrics including Return-to-Axis Probability (RTAP) and Return-to-Origin Probability (RTOP). Immunohistochemical analysis used markers for microglia (Iba1+, CD83), astrocytes (GFAP, AQP4), and neuronal integrity (MAP2**).** Receiver operating characteristic (ROC) analysis evaluated the diagnostic performance of each marker using skeleton analysis protocols. Quantitative morphological analysis employed skeleton analysis protocols comparing the primary somatosensory barrel field cortex (S1BF) and the motor cortex (control). Spatial correspondence was established between dMRI hyperintensity in RTAP and RTOP maps and high concentrations of microglial (Iba1+) pathology in the S1BF. Quantitative analysis revealed significantly higher microglial endpoints and process length in S1BF dense regions compared to the motor cortex. CD83 showed similar regional specificity, providing independent validation of microglial activation patterns. GFAP, AQP4, and MAP2 showed no significant regional differences, suggesting the absence of detectable astrocytic activation or neuronal structural changes at this time point. CD83 endpoints demonstrated the strongest diagnostic performance (AUC = 0.750), while Iba1+ endpoints revealed an inverse

relationship requiring reinterpretation (AUC = 0.816 when properly analyzed), reflecting reduced microglial branching complexity with activation. GFAP, AQP4, and MAP2 showed variable regional differences and poor diagnostic performance, suggesting limited utility as biomarkers at this time point. Imaging confusion matrix analysis demonstrated perfect specificity in control regions but limited sensitivity (33.3%) in injury regions. This study provides the verification of radiologic-pathologic correspondence between dMRI signatures and microglial activation in experimental diffuse TBI. RTAP and RTOP metrics serve as indicators of focal neuroinflammation, supporting their potential as non-invasive biomarkers following brain injury.

Introduction

Traumatic brain injury (TBI) is induced by mechanical forces applied to the head that displace the brain within the skull and disrupt normal neurological function (Lifshitz et al., 2016). TBI represents a significant public health burden, with an estimated 2.87 million emergency department visits, hospitalizations, and deaths occurring annually in the United States alone (Taylor et al., 2017). The economic impact exceeds $40.6 billion annually in healthcare costs for nonfatal traumatic brain injuries alone (Miller et al., 2021), underscoring the critical need for improved diagnostic and prognostic tools.

TBI pathophysiology manifests along a spectrum from focal to diffuse injury patterns. Focal injuries, such as those caused by penetrating wounds or discrete contusions, produce localized tissue damage that is effectively diagnosed using conventional imaging modalities, including computed tomography (CT) and magnetic resonance imaging (MRI). These imaging techniques excel at identifying structural abnormalities such as hemorrhages, contusions, skull fractures, and mass effects in focal TBI, enabling rapid diagnosis, accurate injury characterization, treatment planning, and monitoring of patient outcomes. The success of

conventional imaging in focal TBI has revolutionized emergency medicine and neurosurgical practice, providing clinicians with immediate, non-invasive visualization of injury severity and location.

In contrast, diffuse TBI, the most common form of brain injury, presents a significant diagnostic challenge where these same successful imaging techniques fail to detect pathology. While histological analysis reveals widespread microscopic pathophysiology throughout the brain, this damage occurs without overt structural abnormalities detectable on standard CT or MRI sequences, with studies showing that nonhemorrhagic diffuse axonal injury detection rates are 0% by CT and only 11% by MRI (Lee et al., 2008). Post-mortem tissue analysis readily demonstrates extensive cellular and molecular changes, including diffuse axonal injury, microglial activation, and astrogliosis (Ziebell et al., 2015). However, this histological evidence is limited to invasive post-mortem examination, which provides little benefit for individuals actively suffering from TBI symptomatology who require timely diagnosis and intervention. This creates a critical gap between the known presence of pathological changes demonstrated through tissue analysis and the inability to detect this pathophysiology non-invasively in living patients.

Diffuse TBI is characterized by heterogeneous pathophysiology that varies both between individuals and across brain regions within the same subject. The complex mechanical forces involved in diffuse injury create variable damage patterns that may not be uniform or symmetric between hemispheres (Lifshitz et al., 2016). This spatial and hemispheric heterogeneity presents a significant challenge for conventional imaging techniques, which often fail to detect the subtle but widespread pathological changes characteristic of diffuse TBI. Advanced imaging approaches capable of capturing this heterogeneous pathophysiology are therefore critical for understanding individual injury patterns and developing personalized treatment strategies.

To address this diagnostic limitation, advanced diffusion MRI (dMRI) techniques offer the potential to detect diffuse TBI pathology by enabling the quantification and three-dimensional visualization of water movement within brain tissue. This technique can detect changes in the microenvironment at the cellular level, including alterations in cell size, shape, and tissue organization that may occur following diffuse TBI (Lifshitz et al., 2016). Novel post-image processing techniques enable the extraction of multiple tissue and injury-related contrasts from a single imaging acquisition, providing unprecedented sensitivity to microscale pathophysiological changes. However, dMRI metrics lack specificity, as the imaging signatures are non-specific and require validation against known histopathological markers (Hutchinson et al., 2018).

One of the hallmark characteristics of diffuse TBI pathophysiology is neuroinflammation and the associated microglial activation (Ziebell et al., 2015). Microglia, the resident innate immune cells of the central nervous system, comprise 5-10% of all cells in the brain, and their morphology and function are closely linked (Aguzzi et al., 2013; Shemer et al., 2015; Wolf et al., 2017). In the healthy brain, microglia maintain a ramified morphology characterized by small cell bodies and highly branched processes that continuously survey the extracellular environment (Nimmerjahn et al., 2005; Wake et al., 2009; Tremblay et al., 2011). Following TBI, ramified microglia transition to an activated state, characterized by enlarged cell bodies, thickened and retracted processes, and upregulation of inflammatory markers (Ziebell et al., 2015). Activated microglia orchestrate both degenerative and reparative processes, making them compelling targets for the development of biomarkers.

Recent advances in understanding microglial heterogeneity have revealed additional morphological variants beyond the classical ramified and activated states (Keren-Shaul et al.,

2017; Mathys et al., 2017; Tay et al., 2018; Hammond et al., 2019). Rod microglia represent a distinct activated morphology characterized by elongated cell bodies with processes projecting primarily from apical and basal ends (Taylor et al., 2014). These cells align perpendicular to the cortical surface and form characteristic trains adjacent to neuronal processes (Ziebell et al., 2012; Witcher et al., 2018). Rod microglia have been consistently observed in experimental diffuse TBI models and may represent a specific pathophysiological response to injury that could serve as a biomarker of neuroinflammation (Giordano et al., 2021).

Rod microglia provide insight into their potential functional significance across multiple neurological conditions, having been observed not only in experimental and clinical traumatic brain injury but also in age-related neurodegenerative diseases, including Alzheimer's disease, dementia with Lewy bodies, and hippocampal sclerosis of aging (Giordano et al., 2021; Bachstetter et al., 2015). Following experimental diffuse TBI, rod microglia emerge dynamically as part of the continuous neuroinflammatory response that evolves over the first week post-injury (Ziebell et al., 2017). Rod microglia populations show initial accumulation at acute time points (2 and 6 hours post-injury) and continue to increase, reaching peak populations at 7 days post-injury (DPI) when the morphology is considered fully formed (Taylor et al., 2014; Morrison et al., 2017). This temporal progression reflects the ongoing pathophysiological cascades initiated by the initial injury, with rod microglia formation representing a sustained response to persistent cellular damage and repair processes.

Contemporary microglial activation can be measured *in vivo* using radiolabeled ligands and positron emission tomography (PET) imaging, which provides information about the distribution and intensity of microglial activation (Liu et al., 2019). However, established protocols and techniques cannot provide information about specific microglia morphology or the

cellular microenvironment. Diffusion MRI enables the quantification and visualization of water movement within a voxel, allowing for the detection of changes in the microenvironment at the cellular level to track diffuse TBI pathophysiology.

By establishing a radiologic-pathologic correspondence between dMRI signatures and histological markers of neuroinflammation, we can bridge the gap between observable pathophysiology and non-invasive imaging capabilities. This approach leverages the strengths of both modalities: the cellular specificity of immunohistochemistry and the clinical applicability of advanced MRI techniques. Such verification studies are essential for translating experimental findings into clinically relevant biomarkers that could improve diagnosis, prognosis, and therapeutic monitoring in TBI survivors.

The present study addresses this critical need through two complementary aims that examine radiologic-pathologic correspondence in experimental diffuse TBI. Aim 1 seeks to verify preliminary data suggesting a novel dMRI signature for activated microglia by conducting a cortical survey comparing microglial pathology between the S1BF and motor cortex. This regional comparison leverages the heterogeneous distribution of pathology in diffuse TBI, where the S1BF region was targeted due to its anatomical positioning along the injury pathway and consistent demonstration of injury-related changes, while the motor cortex was selected as a comparative control region with expected minimal injury involvement. We hypothesized that there would be a significant regional difference in microglial activation between S1BF and motor cortex regions. Preliminary research suggests preferential S1BF involvement in diffuse TBI, providing context for expected patterns of regional pathology. Quantitative analysis using Iba1+ immunohistochemistry was performed to assess regional differences in microglial endpoints and process morphology, followed by qualitative comparison of histological findings to regions of

hyperintensity observed in dMRI metrics.

The selection of S1BF and motor cortex regions is based on their differential vulnerability profiles in experimental diffuse TBI models. The S1BF demonstrates consistent and pronounced pathological involvement following midline fluid percussion injury, with progressive neurodegeneration and microglial activation extending from superficial cortical layers to subcortical white matter over the first month post-injury (Lifshitz et al., 2009; Hall et al., 2008). Studies have shown that the somatosensory circuit, including the S1BF, exhibits significantly reduced glucose metabolism and impaired stimulus-evoked responses at both 4 and 24 hours following fluid percussion injury (Ginsberg et al., 1997). Recent studies have confirmed that the S1BF is a primary site of rod microglia formation and sustained neuroinflammation following experimental diffuse TBI, with spatial association between microglial activation and astrogliosis persisting at 7 days post-injury (Witcher et al., 2018).

In contrast, motor cortex regions demonstrate minimal pathological involvement in midline fluid percussion models, which primarily produce diffuse injury patterns without focal cortical (Lifshitz et al., 2016). The midline fluid percussion model is specifically designed to avoid direct motor cortex involvement by positioning the injury centrally over the sagittal suture, thereby creating a diffuse injury pattern that preferentially affects sensory processing regions while sparing primary motor areas (Dixon et al., 1987). This makes the motor cortex an appropriate control region for comparative analysis, allowing validation of dMRI sensitivity to injury-specific pathological changes rather than generalized tissue responses.

Aim 2 explores additional radiologic-pathologic correspondence by examining multiple histopathologic targets of diffuse TBI through immunohistochemical analysis. We assessed regional differences in astrocytic activation (GFAP, AQP4), neuronal dendritic structure

(MAP2), and microglial activation (CD83) between S1BF and motor cortex regions. We hypothesized that additional histopathologic markers would demonstrate the same correspondence with dMRI hyperintensity patterns as microglial markers, thereby validating that the dMRI signature reflects broader cellular pathology beyond microglial activation alone.

Quantitative comparisons between brain regions will be followed by a qualitative assessment of correspondence between histopathological findings and hyperintensity patterns of two different dMRI metrics: Return to Axis Probability (RTAP) and Return to Origin Probability (RTOP). This analysis will establish the cellular basis for the novel dMRI signature and its potential as a biomarker for diffuse TBI pathophysiology.

RTAP and RTOP provide complementary information about tissue microstructural properties and water diffusion behavior (Özarslan et al., 2013). RTAP quantifies the probability that water molecules return to the primary diffusion axis, specifically measuring restriction along the main direction of the diffusion tensor (Özarslan et al., 2013). RTAP has been associated with axonal diameter and tissue microarchitecture, making it valuable for detecting changes in directionally organized pathological processes (Fick et al., 2016).

RTOP reflects the probability that water molecules return to their exact starting position during the diffusion time, providing a measure of overall tissue restriction. In regions with increased cellular density or restricted microenvironments, water molecules are more likely to return to their origin, resulting in higher RTOP values, which are represented as hyperintensity on RTOP maps (Avram et al., 2016).

Methods

Animals

Four adult male Sprague Dawley rats (325-350 g, Charles River Laboratories, Wilmington, MA) were used for all experiments. Three rats underwent experimental diffuse TBI (n = 3), and one was a sham (n = 1). Rats were group-housed in a 12:12 light-dark cycle at a fixed temperature (23°) with food and water available ad libitum according to the Association for Assessment and Accreditation of Laboratory Animal Care International guidelines.

Experimental Diffuse Traumatic Brain Injury

Rats were subjected to midline fluid percussion injury (mFPI). Rats were anesthetized using 5% isoflurane in 100% oxygen for 5 minutes, and their heads were placed in a stereotaxic frame with continuously delivered isoflurane at 2.5% via a nosecone. Body temperature was maintained using a Deltaphase isothermal heating pad (Braintree Scientific, Inc., Braintree, MA). A midline incision was made, exposing bregma and lambda, and the fascia was removed from the surface of the skull. A trephine (4.8 mm outer diameter) was used for the craniectomy, centered on the sagittal suture between bregma and lambda without disruption of the dura. A skull screw was secured in a 1-mm hand-drilled hole in the right frontal bone. An injury cap was prepared from a Luer-Lok needle hub and fixed over the craniectomy using cyanoacrylate gel and methyl-methacrylate (Hygenic Corp., Akron, OH). The incision was sutured at the anterior and posterior edges, and topical Lidocaine ointment and bacitracin were applied. Rats were placed in a heated recovery cage and monitored until ambulatory (Ziebell et al., 2012; Lifshitz et al., 2016).

For injury induction, rats were re-anesthetized (60–90 min after surgery) with 5% isoflurane delivered for 5 minutes. The dura was visually inspected through the hub to ensure

integrity with no debris present. The hub was then filled with normal saline and attached to the fluid percussion device (Custom Design and Fabrication, Virginia Commonwealth University, Richmond, VA). A diffuse brain injury (1.8 - 2.0 atm) was administered by releasing the pendulum onto the fluid-filled cylinder. Rats were monitored for the presence of a forearm fencing response, and righting reflex times were recorded for the injured rats as indicators of injury severity (Lifshitz et al., 2016). The injury hub was removed, and the brain was inspected for uniform herniation and integrity of the dura. Diffuse brain-injured rats (n = 3) exhibited righting reflex recovery times between 5 and 10 minutes, along with a positive fencing response. The incision was cleaned using saline and closed using staples. After spontaneously righting, rats were placed in a heated recovery cage and monitored until ambulatory (approximately 5–15 minutes) before being returned to their home cage. Animal welfare was monitored and documented daily during postoperative care, with adequate measures taken to minimize pain and discomfort.

Ex Vivo Diffusion Magnetic Resonance Imaging and Image Processing

At 7 days post-injury, rats were injected intraperitoneally (i.p.) with Euthasol (0.002 ml/g, Patterson Veterinary, Greeley, CO) and then transcardially perfused with ice-cold 1X PBS, followed by 4% paraformaldehyde (PFA). Brains were left in the skull for *ex vivo* imaging and stored in 4% PFA at 4°C for 5 days. They were then transferred to 0.01% sodium azide in 1X PBS until image acquisition.

Diffusion MRI data were collected using a 40 mm coil with a pre-clinical 7T MRI system (Bruker, Billerica, MA). A customized multi-brain holder designed to accommodate four rat brains simultaneously allowed for efficient parallel imaging. Single-shot echo planar imaging (EPI) was collected in forward and reverse phase directions, and approximately 300 T2-weighted

diffusion-weighted images (DWIs) were acquired across multiple b-values and gradient directions.

Raw T2 DWIs were imported and processed using TORTOISE software (National Institutes of Health, Bethesda, MD) (Pierpaoli et al., 2010). To correct for apparent motion, blip-up/blip-down geometric distortion, and align individual DWIs, the DIFFPREP and DRBUDDI modules were applied (Irfanoglu et al., 2015). Corrected DWIs were then processed using DIFFCALC software in TORTOISE for diffusion tensor fitting and directionally encoded color (DEC) map visualization, resulting in individual diffusion tensor images (DTIs) and DEC maps for each brain. DRTAMAS and DIFFCALC were applied to individual DTIs and DEC maps to build DTI templates (Irfanoglu et al., 2016). DIFFCALC was applied to DTI templates to calculate the metric return-to-axis probability (RTAP) and return-to-origin probability (RTOP) (Özarslan et al., 2013). Diffusion MRI scans were assessed both qualitatively and quantitatively for region-specific alterations in the S1BF and motor cortex.

Immunohistochemistry

After imaging, brains were removed from the skull and cryoprotected in 30% sucrose for 48 hours, then frozen in OCT Compound (Fisher Scientific, Hampton, NH) using isopentane at -20°C. Frozen tissue blocks were transferred to a cryostat, and coronal sections were collected at 20 μm thickness onto glass slides. Sections were stored at -80°C until processing. Slides were defrosted in an oven at 50°C for 2 hours prior to processing.

Sections were hydrated with 1X PBS and then incubated at room temperature overnight with primary antibodies including: 1:500 anti-Iba1+ (ionized calcium-binding adapter protein; FUJIFILM Wako, Richmond, VA) for microglia (Ziebell et al., 2012), 1:500 anti-GFAP (glial

fibrillary acidic protein; clone GA5, Sigma-Aldrich, St. Louis, MO) for astrocytes, 1:500 anti-AQP4 (aquaporin 4; Santa Cruz Biotechnology, Dallas, TX) for astrocyte water channels, 1:1000 anti-MAP2 (microtubule-associated protein 2; BioLegend, San Diego, CA) for neuronal dendrites (Witcher et al., 2018), and 1:200 anti-CD83 (Thermo Fisher Scientific, Waltham, MA) for activated microglia. Secondary antibodies conjugated to biotin (1:250; Vector Laboratories, Burlingame, CA) were incubated for one hour at room temperature. Slides were placed in 1.2% H_2O_2 to block endogenous peroxidases and then incubated with avidin/biotinylated enzyme complex (ABC reagent; Vector Laboratories) for 30 minutes. DAB (Vector Laboratories) was applied to sections and removed once cells became clearly visible under microscopic examination.

Data Analysis

Brightfield images were acquired using a high-resolution slide scanner (Motic EasyScan Pro 6) with 40X EDF objective magnification. Images were stitched together to create complete coronal sections for analysis using Motic EasyScan Pro 6 DSAssistant and EasyScanner software. For quantitative analysis, three non-overlapping square regions of interest (ROIs; 1000 pixels x 1000 pixels) were systematically positioned across the somatosensory barrel field cortex (S1BF) cortical region and motor cortex region.

Microglial morphological analysis was performed using ImageJ software (National Institutes of Health, Bethesda, MD) with skeleton analysis protocols (Morrison & Filosa, 2013; Morrison et al., 2017) to enable automated quantification of cellular architecture. Binary images were generated from immunohistochemically stained sections. Skeleton analysis, an objective and reproducible method for quantifying complex cellular morphologies, measured parameters

including process length and branch endpoints to distinguish between pathological and standard processes.

Statistical analysis was conducted using Microsoft Excel (Microsoft Corporation, Redmond, WA). Paired two-tailed t-tests were performed to compare immunohistochemical measurements between the S1BF cortex region and the motor cortex. Statistical significance was assigned at the 95% confidence level ($\alpha < 0.05$). Qualitative analyses between dMRI metrics and immunohistochemical measurements were performed to describe radiologic-pathologic correspondence.

Receiver Operating Characteristic (ROC) analysis was used to evaluate the ability of endpoints and length of processes (LOP) independently to discriminate between injured and non-injured pathology classifications. The ROC curve was generated by calculating the true positive rate (TPR) and false positive rate (FPR) across a range of thresholds applied to the endpoints or length of processes as separately modeled variables. The Area Under the Curve (AUC) was computed to quantify the overall discriminative ability.

The optimal classification threshold was determined using Youden's Index, selecting the cutoff that maximized this value. A confusion matrix was then produced at this threshold to summarize classification performance in terms of true positives, false positives, true negatives, and false negatives. Plots of the ROC curve and a scatter plot of endpoints or length of processes (LOP)vs actual injury classification (with the threshold indicated) were generated to visualize results. This was done for each antibody using MedCalc.

To evaluate the diagnostic performance of diffusion MRI signatures, a qualitative confusion matrix analysis was performed comparing imaging findings with histologically confirmed injury status. Each region of interest was classified as either imaging-positive

(presence of hyperintensity in RTAP and/or RTOP maps) or imaging-negative (absence of hyperintensity) by visual assessment of diffusion MRI data. Actual injury status was determined based on the presence or absence of histologically confirmed pathological markers, including microglial activation, astrocytic changes, and neuronal structural alterations as assessed through immunohistochemical analysis.

Imaging classification and actual injury status were organized into 2×2 confusion matrices for both primary motor cortex (PMC) and primary somatosensory barrel field cortex (S1BF) regions. Performance metrics, including sensitivity (true positive rate), specificity (true negative rate), precision (positive predictive value), accuracy, and F1 score, were calculated from the confusion matrix data when applicable. PMC served as a control region where minimal injury-related changes were expected, while S1BF represented the primary region of pathological involvement. This analysis enabled assessment of the regional specificity and diagnostic utility of diffusion MRI signatures for detecting injury-induced neuroinflammatory changes.

Results

Sham Animal (n=1)

To establish baseline conditions and validate injury-specific changes, one sham-operated control animal (Brain 5) underwent identical surgical procedures, including craniectomy without fluid percussion injury. This sham control provides a reference standard for interpreting injury-induced alterations in both imaging signatures and histopathological markers. Due to the limited sample size (n=1), this sham control can only serve as a reference point, and no statistical conclusions can be drawn from this data.

Figure 1

Rod microglia distribution in sham (n=1). Coronal brain sections showing rod microglia density in the primary somatosensory barrel field (S1BF) cortex and motor cortex across Brain 5, 7 days post-craniectomy. Rod microglia density was assessed in the primary somatosensory barrel field (S1BF) cortex and motor cortex of each hemisphere and categorized as follows: red regions indicate no rod microglia present; light blue regions indicate 1-10 rod microglia present; medium blue regions indicate 11-20 rod microglia present; dark blue regions indicate >20 rod microglia per region of interest. Scale reference: Interaural 4.56 mm, Bregma - 4.44 mm.

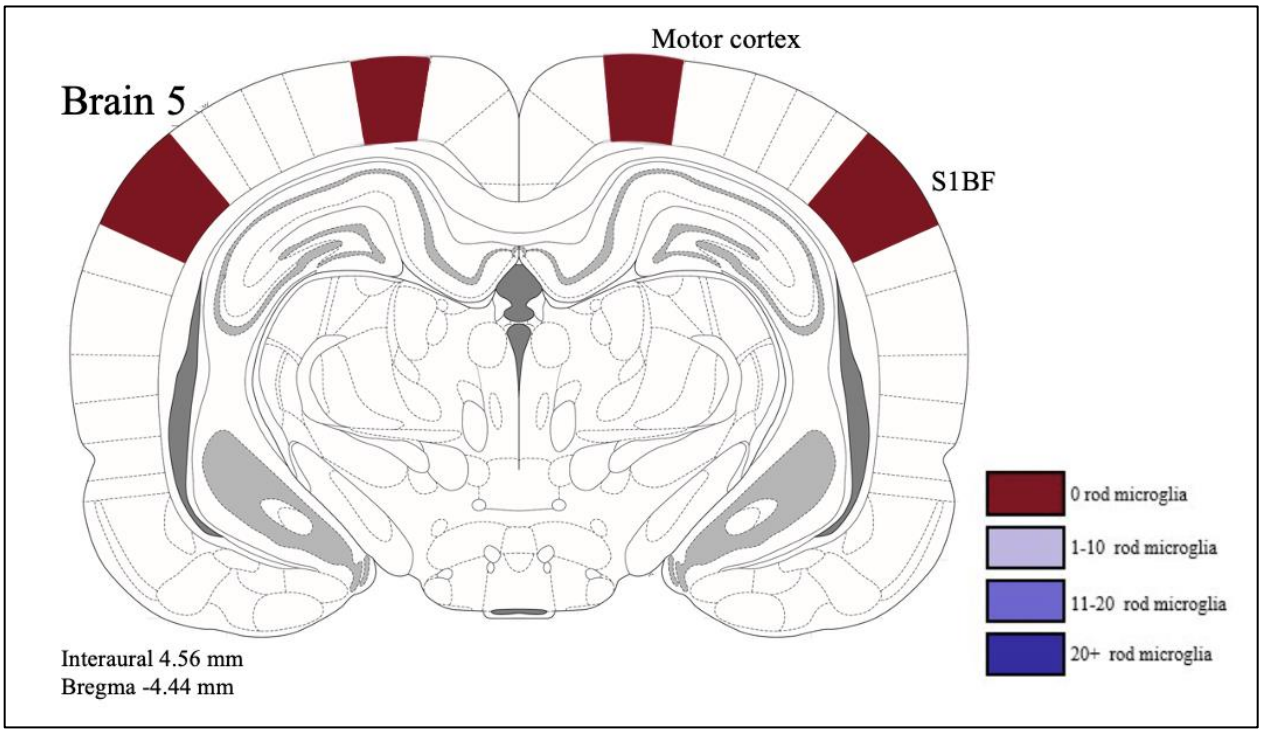

Examination of the sham control brain revealed an absence of rod microglia across all cortical regions examined, with red regions indicating no rod microglia present throughout both S1BF and motor cortex areas in both hemispheres. This observation is consistent with the expected baseline condition in uninjured brain tissue, where rod microglia formation would not be anticipated in the absence of injury-induced pathophysiology.

Figure 2

Regional variation in Iba1+ microglial density within the S1BF following sham (n=1). Representative immunohistochemical staining showing Iba1+ microglia in non-dense (A, C) and dense (B, D) regions of the S1BF across left and right hemispheres for Brain 5. Dense regions demonstrate increased microglial density and activated morphologies compared to non-dense regions. Red circles indicate hemispheres where images were collected in the S1BF but lacked dense pathology and further correspond to minimal rod microglia presence documented in Figure 1.

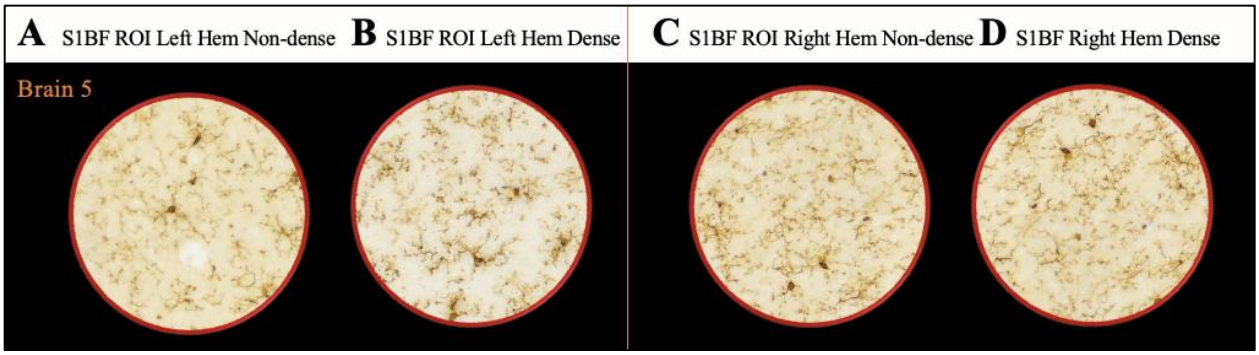

Iba1+ immunohistochemical staining in the sham control demonstrated ramified microglial morphology typical of healthy brain tissue. Unlike the distinct dense and non-dense pathological regions observed in brain-injured animals, the sham control showed uniform microglial distribution without visible clustering or activated morphologies across S1BF regions. The microglia maintained characteristic small cell bodies with extended, highly branched processes consistent with surveillance function in uninjured tissue.

Figure 3

Radiologic-pathologic correspondence between dMRI metrics and microglial pathology in sham (n=1). (A) Return-to-Axis Probability (RTAP) maps, (B) Return-to-Origin Probability (RTOP) maps, and (C) Iba1+ immunohistochemistry showing microglial distribution in Brain 5. Orange arrows indicate regions where hyperintensity in both RTAP and RTOP maps corresponds with dense microglial pathology.

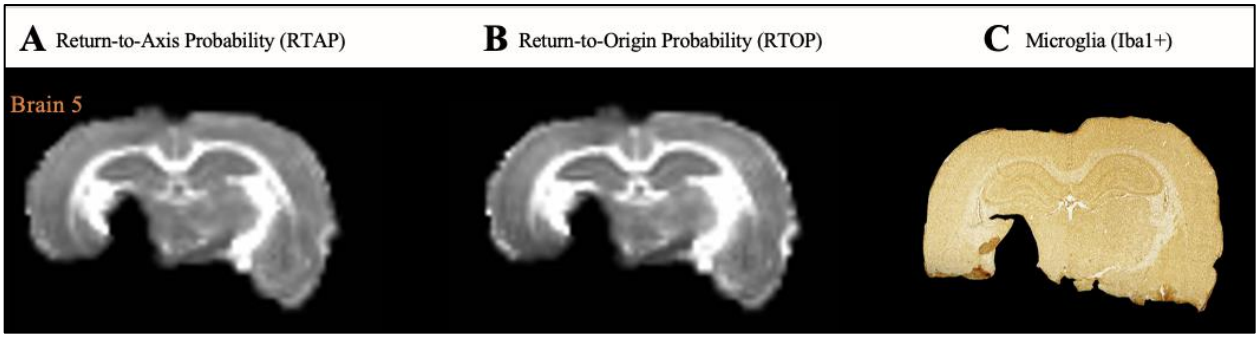

Correspondingly, both RTAP and RTOP diffusion MRI metrics in the sham control showed uniform signal intensity without the hyperintense regions observed in brain-injured animals. The absence of dMRI hyperintensity in S1BF regions parallels the lack of microglial pathology, providing a reference point for comparison with the imaging signatures observed in injured brains.

The sham control provides a reference baseline showing the absence of rod microglia formation, regional microglial activation and clustering, and corresponding dMRI hyperintensity patterns. This reference standard highlights what we are looking for in healthy brain tissue and serves as a comparison point for the changes observed in injured animals.

Rod Microglia Morphology and Distribution

A preliminary investigation between dMRI metrics and diffuse TBI biomarkers focused on rod microglia, a distinct morphological variant of activated microglia, to determine whether a potential imaging signature of hyperintensity in the S1BF corresponded to rod microglia

pathology (Giordano, 2023). Results from that study suggested that the potential biomarker of diffuse TBI may instead reflect activated microglia more broadly. In the present study, Iba1+-immunostained brain sections revealed the presence of rod microglia across select regions of the S1BF (Brain 3, Brain 4, Brain 6) at 7 days post-injury (Figure 1). Rod microglia were characterized by their elongated cell bodies with processes projecting primarily from apical and basal ends, aligned perpendicular to the cortical surface, and typically forming characteristic trains adjacent to neuronal processes.

Figure 4

Rod microglia distribution across experimental brains following diffuse traumatic brain injury. Coronal brain sections showing rod microglia density in the primary somatosensory barrel field (S1BF) cortex and motor cortex across Brain 3, Brain 4, and Brain 6 at 7 days post-injury. Rod microglia density was assessed in the primary somatosensory barrel field (S1BF) cortex and motor cortex of each hemisphere and categorized as follows: red regions indicate no rod microglia present; light blue regions indicate 1-10 rod microglia present; medium blue regions indicate 11-20 rod microglia present; dark blue regions indicate >20 rod microglia per region of interest. Scale reference: Interaural 4.56 mm, Bregma - 4.44 mm.

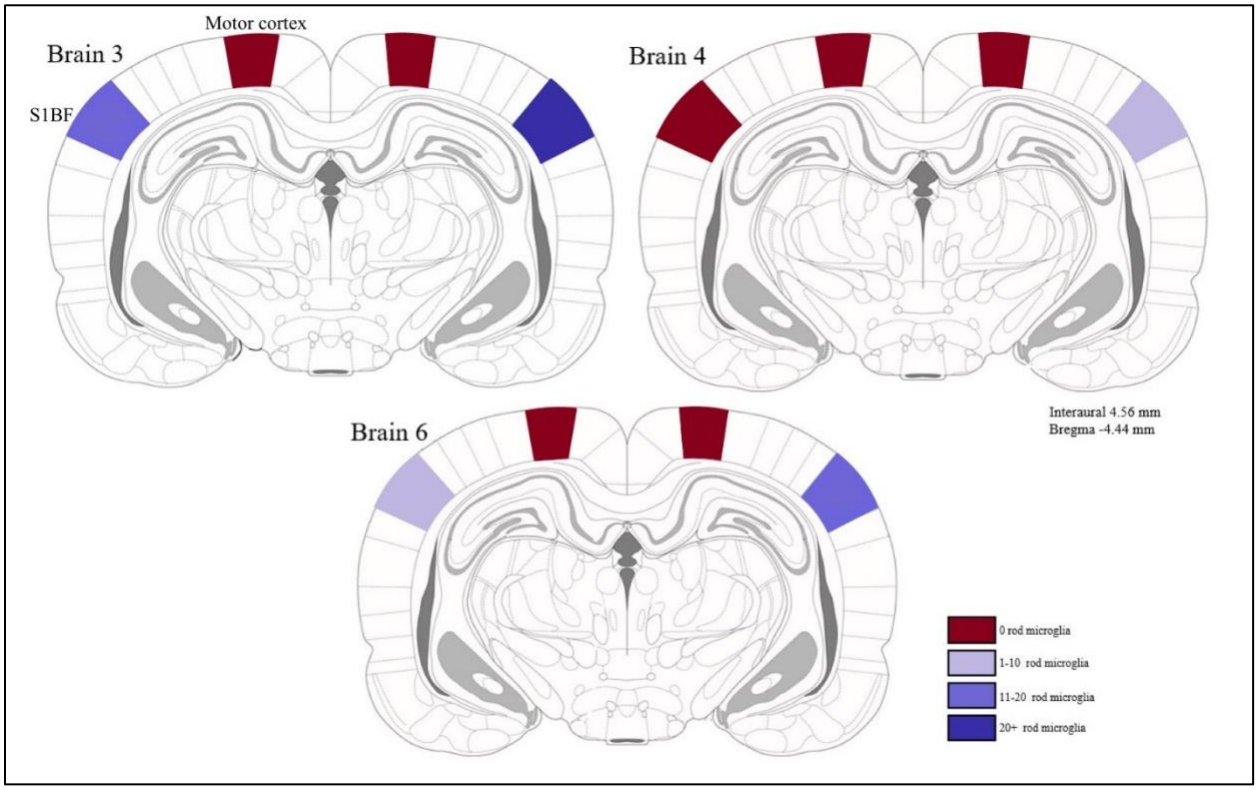

The distribution and density of rod microglia varied between S1BF and motor cortex regions, as well as between hemispheres within each brain. Rod microglia were predominantly observed in S1BF regions, with motor cortex showing no rod microglia presence across all experimental brains. Within the S1BF, areas of dense rod microglia pathology (>20 rod microglia) were interspersed with regions of lower density (1-20 rod microglia) or absent rod microglia, creating a heterogeneous distribution pattern. This morphological assessment

provided crucial context for understanding the regional specificity of injury pathophysiology present in our experimental model and established the foundation for subsequent quantitative analyses comparing dense versus non-dense pathological regions within S1BF and motor cortex controls.

Aim 1: Regional Differences in Microglial Activation

Based on the heterogeneous distribution of rod microglia observed in Figure 1, quantitative analysis of Iba1+ microglia was designed to compare three distinct area types: regions within S1BF showing high concentrations of activated microglia (dense regions), adjacent areas within S1BF with lower microglial concentrations (non-dense regions), and motor cortex regions serving as controls due to no rod microglia presence, as seen in Figure 1. This analytical approach was developed to determine whether the observed heterogeneity in rod microglia distribution corresponds to broader patterns of microglial activation. Following TBI, microglial morphology undergoes characteristic changes with activation, resulting in an accumulation of activated microglia within the S1BF (Ziebell et al., 2012; Morrison et al., 2017). Distinct spatial patterns emerge, including regions where activated microglia and rod microglia variants congregate at high density, as well as adjacent areas within the same cortical region where microglial density remains closer to uninjured levels (Figure 2).

Figure 5

Regional variation in Iba1+ microglial density within the S1BF following diffuse traumatic brain injury. Representative immunohistochemical staining showing Iba1+ microglia in non-dense (A, C) and dense (B, D) regions of the S1BF across left and right hemispheres for Brains 3, 4, and 6. Dense regions demonstrate increased microglial density and activated morphologies compared to non-dense regions. Red circles indicate hemispheres where images were collected in the S1BF but lacked dense pathology and further correspond to minimal rod microglia presence documented in Figure 1.

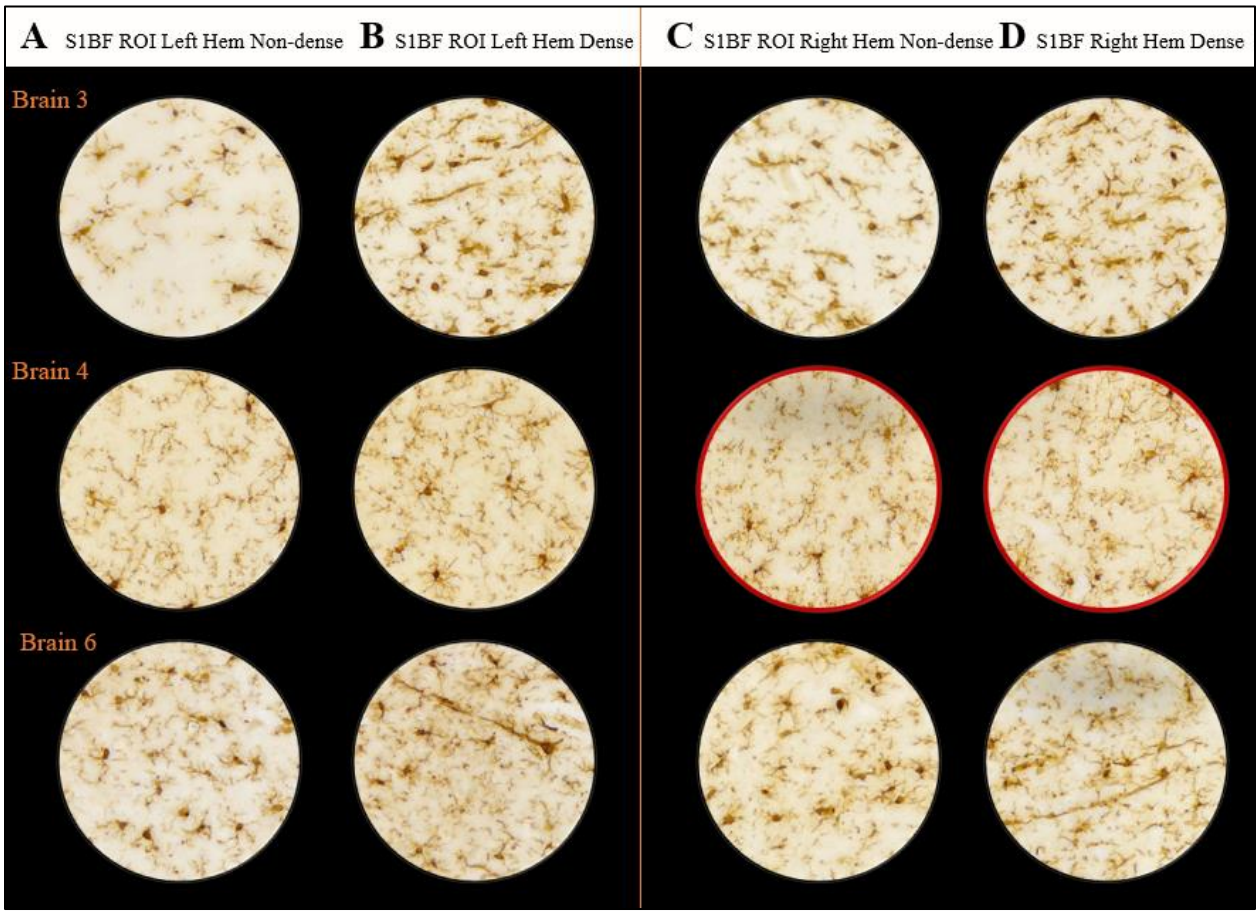

Both dense and non-dense regions within the S1BF were analyzed to determine whether morphological differences existed between areas of varying microglial density within this cortical region. Dense and non-dense regions within the S1BF were identified through systematic visual assessment of Iba1+ immunostaining patterns by examining whole coronal sections at 40x magnification. Dense regions were characterized as 1000×1000 pixel ROIs where activated and

rod microglia appeared concentrated with high cellular density and clustered distribution patterns. Non-dense regions were ROIs immediately adjacent to dense regions where microglial density appeared visibly lower with more dispersed cellular organization.

The variation in microglial density observed within the S1BF in Figure 2 corresponds with the rod microglia density patterns documented within the same region in Figure 1, demonstrating consistent spatial organization of neuroinflammatory responses between different microglial markers. Notably, hemispheres from brain-injured rats showing minimal dense microglial pathology in Figure 2 (indicated by red circles) align with the same hemispheres lacking substantial rod microglia presence in Figure 1, confirming the correspondence between different markers of microglial activation within the S1BF region following diffuse TBI.

Additionally, comparative analysis was conducted between S1BF pathology and the motor cortex to establish regional specificity. Based on preliminary findings, hyperintensity was anticipated within the S1BF, and histopathological comparison between the S1BF and regions lacking hyperintensity was performed to confirm radiologic-pathologic correspondence between MRI signatures and microglial distribution patterns.

Microglia was quantified using two primary metrics: endpoints and length of processes (LOP). Endpoints represent the number of terminal branches on microglial processes, providing a measure of morphological complexity (Morrison & Filosa, 2013). In contrast, LOP quantifies the total cumulative length of all processes combined, reflecting the overall extent of microglial territorial coverage (Young & Morrison, 2018). These morphological parameters were obtained using established skeleton analysis protocols that convert immunostained microglial images into skeletal representations for automated quantification (Morrison et al., 2017).

For left hemisphere non-dense regions, a paired, two tailed T-test was conducted to compare endpoint values between S1BF and motor cortex regions. There was no statistically significant difference between S1BF (M = 1811.56, SD = 262.26) and motor cortex (M = 1411.33, SD = 68.02), $t(2) = 3.28$, $p = 0.08$ (Table 1). Additionally, a paired, two tailed T-test was conducted to compare length of process values between S1BF and motor cortex regions. There was a statistically significant difference between S1BF (M = 25778.07, SD = 4124.84) and motor cortex (M = 18352.86, SD = 1712.27), $t(2) = 4.67$, $p = 0.04$ (Table 1).

For left hemisphere dense regions, a paired, two tailed T-test was conducted to compare endpoint values between S1BF and motor cortex regions. There was a statistically significant difference between S1BF (M = 2178.89, SD = 158.45) and motor cortex (M = 1411.33, SD = 68.02), $t(2) = 5.95$, $p = 0.03$ (Table 1). Additionally, a paired, two tailed T-test was conducted to compare length of process values between S1BF and motor cortex regions. There was a statistically significant difference between S1BF (M = 27908.35, SD = 2810.90) and motor cortex (M = 18352.86, SD = 1712.27), $t(2) = 13.12$, $p = 0.006$. (Table 1).

Table 1

Quantitative analysis of Iba1+ microglia in left hemisphere regions following diffuse traumatic brain injury. Data presented as mean ± standard deviation in primary somatosensory barrel field cortex (S1BF) compared to motor cortex regions. Endpoint values represent number of terminal branches per region of interest (ROI). LOP = Length of Processes (μm). Statistical analysis was performed using paired t-test with significance set at α = 0.05. n = 3 brains per comparison.

Brain ID	**S1BF Non-Dense**		**S1BF Dense**		**Motor Cortex**	
	Endpoint	LOP	Endpoint	LOP	Endpoint	LOP
3	1606.83	23765.45	2131.33	24855.06	1403.33	16754.39
4	2107.17	30522.87	2049.67	30388.51	1483.00	20159.84
6	1720.67	23045.86	2355.67	28481.49	1347.67	18144.35
Mean	**1811.56**	**25778.06**	**2178.89**	**27908.35**	**1411.33**	**18352.86**

For right hemisphere non-dense regions, a paired, two tailed T-test was conducted to compare endpoint values between S1BF and motor cortex regions. There was no statistically significant difference between S1BF (M = 1834.34, SD = 341.60) and motor cortex (M = 1571.67, SD = 451.41), $t(2) = 2.64$, $p = 0.12$ (Table 2). Additionally, a paired, two tailed T-test was conducted to compare length of process values between S1BF and motor cortex regions. There was a statistically significant difference between S1BF (M = 26804.14, SD = 3944.73) and motor cortex (M = 15942.25, SD = 2655.95), $t(2) = 14.46$, $p = 0.005$ (Table 2).

For right hemisphere dense regions, a paired, two tailed T-test was conducted to compare endpoint values between S1BF and motor cortex regions. There was no statistically significant difference between S1BF (M = 2098.45, SD = 168.14) and motor cortex (M = 1571.67, SD = 451.41), $t(2) = 2.38$, $p = 0.14$ (Table 2). Additionally, a paired, two tailed T-test was conducted to compare length of process values between S1BF and motor cortex regions. There was a statistically significant difference between S1BF (M = 28776.79, SD = 1202.61) and motor cortex (M = 15942.25, SD = 2655.95), $t(2) = 15.22$, $p = 0.004$ (Table 2).

Table 2

Quantitative analysis of Iba1+ microglia in right hemisphere regions following diffuse traumatic brain injury. Data presented as mean ± standard deviation in primary somatosensory barrel field cortex (S1BF) compared to motor cortex regions. Endpoint values represent number of terminal branches per region of interest (ROI). LOP = Length of Processes (μm). Statistical analysis was performed using paired t-test with significance set at α = 0.05. n = 3 brains per comparison.

Brain ID	**S1BF Non-Dense**		**S1BF Dense**		**Motor Cortex**	
	Endpoint	LOP	Endpoint	LOP	Endpoint	LOP
3	1494.50	22307.34	1905.33	27411.96	1236.67	12892.48
4	1783.68	23543.73	2177.68	29681.02	2085.00	17746.91
6	1830.83	28424.07	2212.33	29237.38	1393.33	17187.34
Mean	**1834.34**	**26804.14**	**2098.45**	**28776.79**	**1571.67**	**15942.25**

Qualitative analysis was conducted to examine the radiologic-pathologic correspondence between microglia (Iba1+) and diffusion MRI frameworks using MAP-MRI metrics Return-to-Axis Probability (RTAP) and Return-to-Origin Probability (RTOP). This analysis aimed to visually assess gross pathological correspondences between regions of hyperintensity in RTAP and RTOP maps and microglial activation patterns following diffuse traumatic brain injury.

The hyperintensity observed in both RTAP and RTOP maps within the S1BF region suggests the presence of microstructural alterations that restrict water diffusion both generally (RTOP) and along specific axes (RTAP). These imaging signatures correspond spatially with regions of increased microglial density and activation, as confirmed by subsequent immunohistochemical analysis (Figure 3). The complementary nature of these metrics provides enhanced sensitivity for detecting neuroinflammatory changes, as RTOP captures overall tissue restriction while RTAP specifically identifies directional microstructural organization that may reflect specific pathological processes such as microglial alignment or axonal injury (Le et al., 2020).

Visual assessment of dMRI metrics revealed a spatial correspondence between regions of hyperintensity in RTAP and RTOP maps and areas of dense microglial pathology (Figure 3). As indicated by the orange arrows in Figure 3, hyperintensity in both RTAP (Panel A) and RTOP (Panel B) maps was observed exclusively in regions that demonstrated dense Iba1+ microglial staining (Panel C). This correspondence was consistently observed across subjects with robust pathological changes.

Figure 6

Radiologic-pathologic correspondence between dMRI metrics and microglial pathology. (A) Return-to-Axis Probability (RTAP) maps, (B) Return-to-Origin Probability (RTOP) maps, and (C) Iba1+ immunohistochemistry showing microglial distribution in Brains 3, 4, and 6. Orange arrows indicate regions where hyperintensity in both RTAP and RTOP maps corresponds with dense microglial pathology.

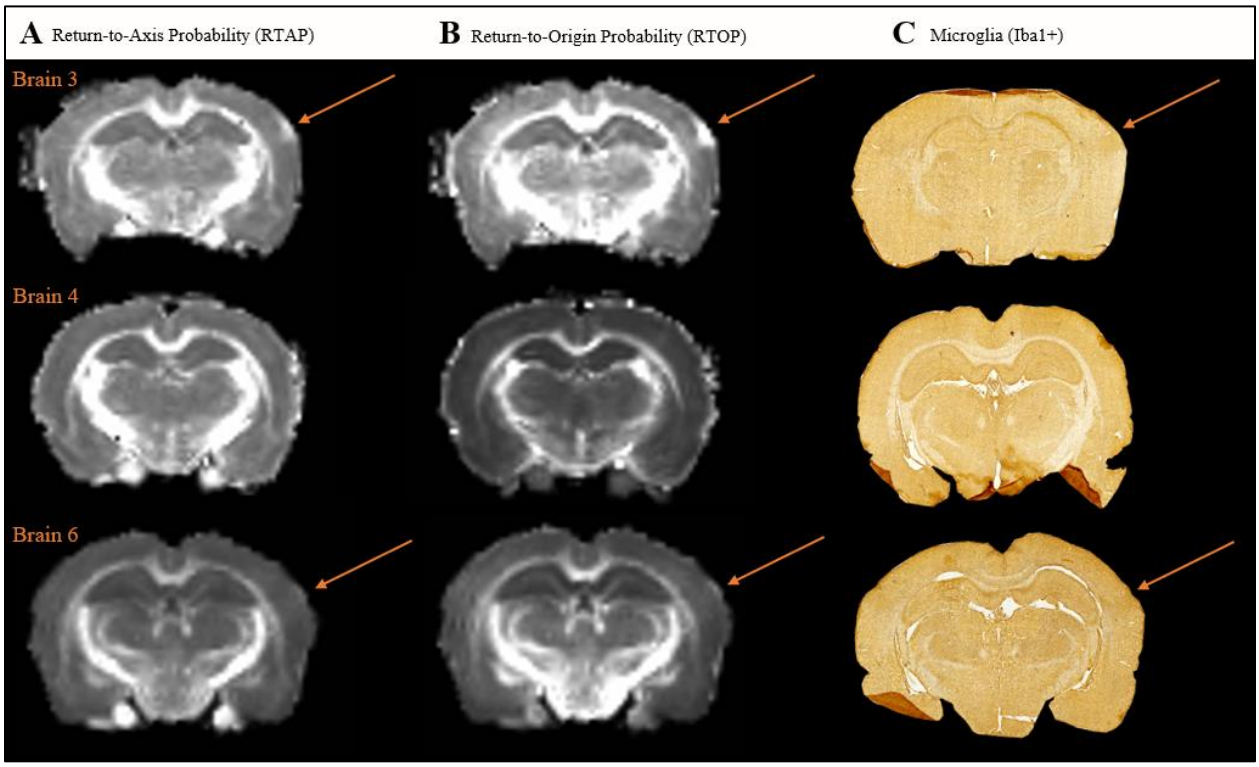

The radiologic-pathologic correspondence demonstrated regional specificity and pathological selectivity. In Brain 3 and Brain 6, where dense microglial pathology with rod microglia presence was evident, corresponding hyperintensity was clearly visible in both dMRI metrics. Conversely, Brain 4 showed minimal to absent hyperintensity in RTAP and RTOP maps, which corresponded directly to activated microglia pathology (Figure 2) in these regions. This selective correspondence suggests that dMRI hyperintensity is specifically associated with regions of significant neuroinflammatory activity rather than reflecting general tissue changes.

Aim 2: Additional Histopathologic Markers of Neuroinflammation and Their Relationship to Diffusion MRI Signatures

While Aim 1 established a radiologic-pathologic correspondence between activated microglia and dMRI hyperintensity, diffuse TBI triggers a complex cascade of neuroinflammatory responses involving multiple cellular and molecular pathways. To evaluate diffusion MRI to detect various aspects of histopathologic markers of diffuse TBI, we expanded our immunohistochemical analysis to include four additional markers representing diverse cellular populations and pathological processes associated with diffuse TBI.

The selected antibodies target distinct components of the neuroinflammatory response: AQP4 (aquaporin-4) for astrocytic water channel expression and potential edema, GFAP (glial fibrillary acidic protein) for astrocytic activation and reactive gliosis, CD83 for activated microglia and dendritic cells, and MAP2 (microtubule-associated protein 2) for neuronal structural integrity. These histopathologic targets represent multiple markers that characterize cells and processes involved in diffuse TBI pathophysiology.

Microglial architecture was quantified using two primary metrics: endpoints (number of terminal branches on microglial processes) and length of processes (LOP), which reflect morphological complexity and territorial coverage, respectively (Morrison & Filosa, 2013; Young & Morrison, 2018). Paired two-tailed t-tests were used to compare measurements between S1BF and motor cortex regions ($\alpha < 0.05$).

Figure 7

Skeleton analysis of histopathologic markers of diffuse traumatic brain injury. (A-D) Representative immunohistochemical staining showing cellular morphology for AQP4 (A), GFAP (B), CD83 (C), and MAP2 (D). (E-H) Corresponding skeleton analysis images demonstrating the automated conversion of immunostained structures to skeletonized representations for quantitative analysis of AQP4 (E), GFAP (F), CD83 (G), and MAP2 (H).

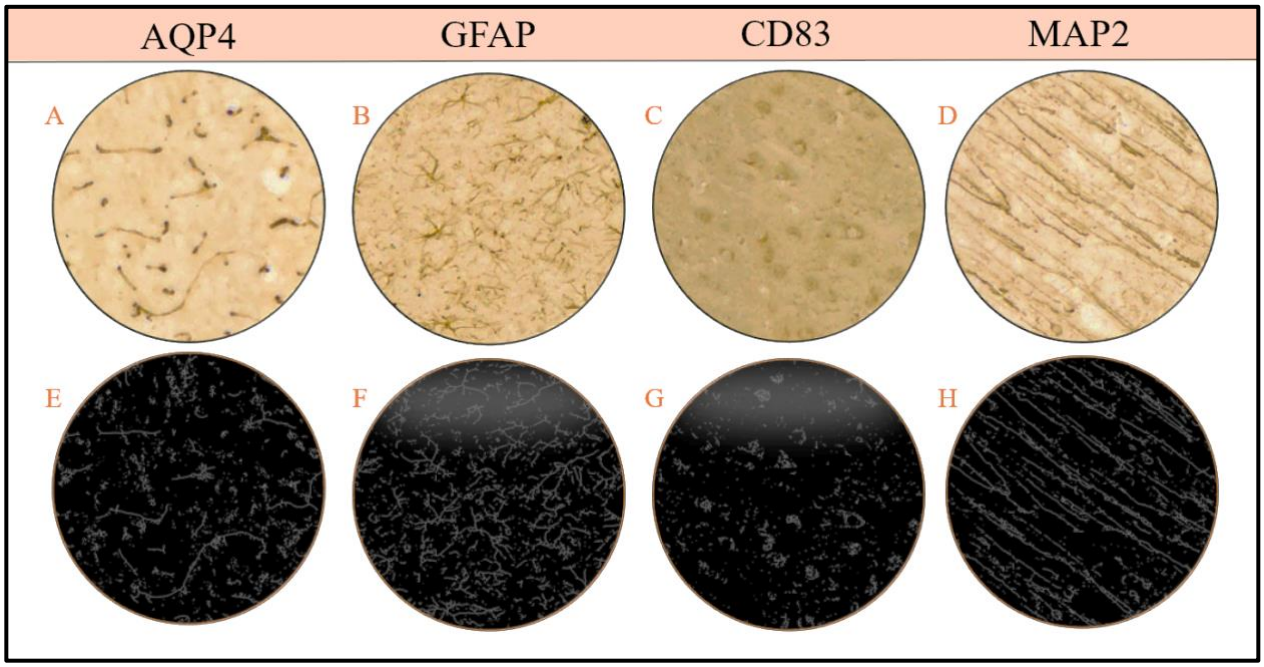

To study the quantification of these neuroinflammatory markers, we compared the individual S1BF regions per hemisphere, where dMRI hyperintensity was consistently observed, to the individual motor cortices of each hemisphere. The motor cortex a cortical region that lacks hyperintensity on RTAP and RTOP maps. This regional comparison approach allows us to

determine whether the imaging signatures detected in the S1BF reflect broader pathophysiology of diffuse TBI beyond microglial activation. The purpose of this analysis was to explore additional radiologic-pathologic correspondence among diverse histopathologic targets of diffuse TBI and dMRI metrics through quantitative immunohistochemistry. By examining these multiple neuroinflammatory markers between regions with and without dMRI hyperintensity, we aimed to determine whether the diffusion signatures observed in Aim 1 reflect specific microglial activation or broader neuroinflammatory processes encompassing multiple cellular populations.

Table 3

Quantitative analysis of histopathologic markers of diffuse traumatic brain injury in left hemisphere regions following experimental diffuse traumatic brain injury. Data presented as mean ± standard deviation for AQP4 (aquaporin-4), in primary somatosensory barrel field cortex (S1BF) compared to motor cortex regions. Endpoint values represent the number of terminal branches per region of interest (ROI). LOP = Length of Processes (μm). Statistical analysis was performed using a paired t-test with significance set at α = 0.05. n = 3 brains per comparison.

Brain ID	**AQP4**			
	S1BF Endpoint	Motor Cortex Endpoint	S1BF LOP	Motor Cortex LOP
3	5059.67	1507.17	31146.82	9342.84
4	2523.14	897.50	33589.17	8372.29
6	2480.50	1543.33	19668.30	9709.37
Mean	**9354.44**	**1316.00**	**28134.76**	**9141.50**

For AQP4 left hemisphere regions a paired, two tailed T-test was conducted to compare endpoint values between S1BF and motor cortex regions. There was no statistically significant difference between S1BF (M = 9354.44, SD = 9757.97) and moto cortex (M = 1316.0, SD = 362.88), $t(2) = 1.38$, $p = 0.30$ (Table 3). Additionally, a paired, two tailed T-test was conducted to compare length of process values between S1BF and motor cortex regions. There was no statistically significant difference between S1BF (M = 28134.77, SD = 7433.17) and motor cortex (M = 7474.84, SD = 3557.63), $t(2) = 3.52$, $p = 0.07$. (Table 3).

Table 4

Quantitative analysis of histopathologic markers of diffuse traumatic brain injury in left hemisphere regions following experimental diffuse traumatic brain injury. Data presented as mean ± standard deviation for GFAP (glial fibrillary acidic protein), in primary somatosensory barrel field cortex (S1BF) compared to motor cortex regions. Endpoint values represent the number of terminal branches per region of interest (ROI). LOP = Length of Processes (μm). Statistical analysis was performed using a paired t-test with significance set at α = 0.05. n = 3 brains per comparison.

Brain ID	**GFAP**			
	S1BF Endpoint	Motor Cortex Endpoint	S1BF LOP	Motor Cortex LOP
3	2904.33	3386.50	24198.93	28587.92
4	3148.33	3114.67	31285.06	23008.52
6	3656.00	3996.00	31626.38	25261.69
Mean	**3236.22**	**3499.06**	**29036.79**	**25619.38**

For GFAP left hemisphere regions, a paired, two tailed T-test was conducted to compare endpoint values between S1BF and motor cortex regions. There was no statistically significant difference between S1BF (M = 3236.39, SD = 383.25) and motor cortex (M = 3499.06, SD = 451.32), $t(2) = 1.71$, $p = 0.23$ (Table 4). Additionally, a paired, two tailed T-test was conducted to compare length of process values between S1BF and motor cortex regions. There was no statistically significant difference between S1BF (M = 29020.79, SD = 4220.87) and motor cortex (M = 25619.38, SD = 2806.84), $t(2) = 0.86$, $p = 0.48$ (Table 4).

Table 5

Quantitative analysis of histopathologic markers of diffuse traumatic brain injury in left hemisphere regions following experimental diffuse traumatic brain injury. Data presented as mean ± standard deviation for CD83 (cluster of differentiation 83), in primary somatosensory barrel field cortex (S1BF) compared to motor cortex regions. Endpoint values represent the number of terminal branches per region of interest (ROI). LOP = Length of Processes (μm). Statistical analysis was performed using a paired t-test with significance set at α = 0.05. n = 3 brains per comparison.

Brain ID	**CD83**			
	S1BF Endpoint	Motor Cortex Endpoint	S1BF LOP	Motor Cortex LOP
3	4319.67	1911.83	23277.73	7899.50
4	3366.67	1571.38	18145.27	6906.76
6	3088.83	1876.50	19068.91	8236.03
Mean	**3591.72**	**1786.72**	**20163.97**	**7680.76**

For CD83 left hemisphere regions, a paired, two tailed T-test was conducted to compare endpoint values between S1BF and motor cortex regions. There was a statistically significant difference between S1BF (M = 3591.72, SD = 645.54) and motor cortex (M = 1786.72, SD = 186.94), $t(2) = 5.23$, $p = 0.03$ (Table 5). Additionally, a paired, two tailed T-test was conducted to compare length of process values between S1BF and motor cortex regions. There was a statistically significant difference between S1BF (M = 29020.79, SD = 4220.87) and motor cortex (M = 7680.41, SD = 691.69), $t(2) = 8.60$, $p = 0.01$ (Table 5).

Table 6

Quantitative analysis of histopathologic markers of diffuse traumatic brain injury in left hemisphere regions following experimental diffuse traumatic brain injury. Data presented as mean ± standard deviation for MAP2 (microtubule-associated protein 2), in primary somatosensory barrel field cortex (S1BF) compared to motor cortex regions. Endpoint values represent the number of terminal branches per region of interest (ROI). LOP = Length of Processes (μm). Statistical analysis was performed using a paired t-test with significance set at α = 0.05. n = 3 brains per comparison.

Brain ID	**MAP2**			
	S1BF Endpoint	Motor Cortex Endpoint	S1BF LOP	Motor Cortex LOP
3	4480.83	4686.33	24500.70	24013.70
4	4485.33	4196.67	28807.30	23902.85
6	2973.00	4740.17	28117.98	30655.93
Mean	**3979.72**	**4541.06**	**27141.99**	**26190.83**

For MAP2 left hemisphere regions a paired, two tailed T-test was conducted to compare endpoint values between S1BF and motor cortex regions. There was no statistically significant difference between S1BF (M = 3979.72, SD = 871.85) and motor cortex (M = 4541.06, SD = 299.46), $t(2) = 0.91$, $p = 0.46$ (Table 6). Additionally, a paired, two tailed T-test was conducted to compare length of process values between S1BF and motor cortex regions. There was no statistically significant difference between S1BF (M = 27142.08, SD = 2313.10) and motor cortex (M = 26271.46, SD = 4005.31), $t(2) = 0.39$, $p = 0.73$ (Table 6).

Table 7

Quantitative analysis of histopathologic markers of diffuse traumatic brain injury in right hemisphere regions following experimental diffuse traumatic brain injury. Data presented as mean ± standard deviation for AQP4 (aquaporin-4) in primary somatosensory barrel field cortex (S1BF) compared to motor cortex regions. Endpoint values represent the number of terminal branches per region of interest (ROI). LOP = Length of Processes (μm). Statistical analysis was performed using a paired t-test with significance set at α = 0.05. n = 3 brains per comparison.

Brain ID	**AQP4**			
	S1BF Endpoint	Motor Cortex Endpoint	S1BF LOP	Motor Cortex LOP
3	5555.83	1209.33	29610.63	5714.05
4	4529.00	1413.67	32723.83	6053.35
6	2221.50	993.67	18945.03	6785.27
Mean	**4102.11**	**1205.56**	**27093.16**	**6184.22**

For AQP4 right hemisphere regions, a paired, two tailed T-test was conducted to compare endpoint values between S1BF and motor cortex regions. There was no statistically significant difference between S1BF (M = 4102.11, SD = 1707.67) and motor cortex (M = 1205.56, SD = 210.03), $t(2) = 3.19$, $p = 0.09$ (Table 7). Additionally, a paired, two tailed T-test was conducted to compare length of process values between S1BF and motor cortex regions. There was a statistically significant difference between S1BF (M = 27093.17, SD = 7226.13) and motor cortex (M = 6184.35, SD = 547.31), $t(2) = 4.70$, $p = 0.04$ (Table 7).

Table 8

Quantitative analysis of histopathologic markers of diffuse traumatic brain injury in right hemisphere regions following experimental diffuse traumatic brain injury. Data presented as mean ± standard deviation for GFAP (glial fibrillary acidic protein) in primary somatosensory barrel field cortex (S1BF) compared to motor cortex regions. Endpoint values represent the number of terminal branches per region of interest (ROI). LOP = Length of Processes (μm). Statistical analysis was performed using a paired t-test with significance set at α = 0.05. n = 3 brains per comparison.

Brain ID	**GFAP**			
	S1BF Endpoint	Motor Cortex Endpoint	S1BF LOP	Motor Cortex LOP
3	2685.17	3198.33	26300.52	27457.09
4	3249.00	3740.83	32268.95	26733.19
6	3589.00	4141.00	30787.89	26597.00
Mean	**3174.39**	**3693.39**	**29785.79**	**26929.09**

For GFAP right hemisphere regions, a paired, two tailed T-test was conducted to compare endpoint values between S1BF and motor cortex regions. There was a statistically significant difference between S1BF (M = 3174.39, SD = 456.51) and motor cortex (M = 3693.39, SD = 473.12), $t(2) = 29.47$, $p = 0.001$ (Table 8). Additionally, a paired, two tailed T-test was conducted to compare length of process values between S1BF and motor cortex regions. There was no statistically significant difference between S1BF (M = 29785.91, SD = 3107.63) and motor cortex (M = 26359.10, SD = 534.36), $t(2) = 2.30$, $p = 0.15$ (Table 8).

Table 9

Quantitative analysis of histopathologic markers of diffuse traumatic brain injury in right hemisphere regions following experimental diffuse traumatic brain injury. Data presented as mean ± standard deviation for CD83 (cluster of differentiation 83) in primary somatosensory barrel field cortex (S1BF) compared to motor cortex regions. Endpoint values represent the number of terminal branches per region of interest (ROI). LOP = Length of Processes (μm). Statistical analysis was performed using a paired t-test with significance set at α = 0.05. n = 3 brains per comparison.

Brain ID	**CD83**			
	S1BF Endpoint	Motor Cortex Endpoint	S1BF LOP	Motor Cortex LOP
3	5044.00	1444.00	22915.34	5582.58
4	3273.83	1368.83	23000.65	6493.37
6	3064.33	2466.00	18615.34	11172.05
Mean	**3794.05**	**1759.61**	**21510.44**	**7749.33**

For CD83 right hemisphere regions, a paired, two tailed T-test was conducted to compare endpoint values between S1BF and motor cortex regions. There was no statistically significant difference between S1BF (M = 3794.06, SD = 1087.54) and motor cortex (M = 1759.61, SD = 612.90), $t(2) = 2.34$, $p = 0.14$ (Table 9). Additionally, a paired, two tailed T-test was conducted to compare length of process values between S1BF and motor cortex regions. There was a statistically significant difference between S1BF (M = 21510.44, SD = 2507.59) and motor cortex (M = 7749.47, SD = 2998.88), $t(2) = 4.34$, $p = 0.04$ (Table 9).

Table 10

Quantitative analysis of histopathologic markers of diffuse traumatic brain injury in right hemisphere regions following experimental diffuse traumatic brain injury. Data presented as mean ± standard deviation for MAP2 (microtubule-associated protein 2) in primary somatosensory barrel field cortex (S1BF) compared to motor cortex regions. Endpoint values represent the number of terminal branches per region of interest (ROI). LOP = Length of Processes (μm). Statistical analysis was performed using a paired t-test with significance set at α = 0.05. n = 3 brains per comparison.

Brain ID	**MAP2**			
	S1BF Endpoint	Motor Cortex Endpoint	S1BF LOP	Motor Cortex LOP
3	5281.83	5041.67	31595.84	24577.96
4	4063.83	3373.67	29590.08	24111.14
6	3241.17	4258.83	28627.9	29806.82
Mean	**4195.61**	**4224.72**	**29937.94**	**26165.31**

For MAP2 right hemisphere regions, a paired, two tailed T-test was conducted to compare endpoint values between S1BF and motor cortex regions. There was no statistically significant difference between S1BF (M = 4195.61, SD = 1026.70) and motor cortex (M = 4224.72, SD = 834.52), $t(2) = 0.06$, $p = 0.96$ (Table 10). Additionally, a paired, two tailed T-test was conducted to compare length of process values between S1BF and motor cortex regions. There was a statistically significant difference between S1BF (M = 29937.94, SD = 1514.24) and motor cortex (M = 26155.18, SD = 3169.93), $t(2) = 1.50$, $p = 0.27$ (Table 10).

Receiver Operating Characteristic (ROC) Analysis

To evaluate the diagnostic utility of individual histopathologic markers for distinguishing between injured and non-injured tissue classifications, receiver operating characteristic (ROC) analysis was performed for both endpoints and length of processes metrics across all antibody markers. ROC analysis provides a comprehensive assessment of diagnostic performance by plotting the true positive rate (sensitivity) against the false positive rate across all possible classification thresholds. The area under the ROC curve (AUC) quantifies overall discriminative ability, with values ranging from 0.5 (no discriminative ability, equivalent to random chance) to 1.0 (perfect discrimination).

For each marker, the optimal classification threshold was determined using Youden's Index, which maximizes the sum of sensitivity and specificity. Confusion matrices were generated at these optimal thresholds to summarize classification performance in terms of true positives, false positives, true negatives, and false negatives, enabling calculation of sensitivity, specificity, and overall accuracy for each histopathologic marker.

Figure 8.

ROC analysis and confusion matrices for AQP4 as a predictor of injury classification. (A) Confusion matrix for AQP4 endpoints with true positives (TP) = 20, false negatives (FN) = 16, false positives (FP) = 0, and true negatives (TN) = 12. (B) ROC curve for AQP4 endpoints with an area under the curve (AUC) of 0.694. Red horizontal line indicates the optimal classification threshold at sensitivity = 55.6%. (C) ROC curve for AQP4 length of processes with an AUC of 0.553. Red horizontal line indicates the optimal classification threshold at sensitivity = 75.0%. (D) Confusion matrix for AQP4 length of processes with true positives (TP) = 27, false negatives (FN) = 9, false positives (FP) = 6, and true negatives (TN) = 6.

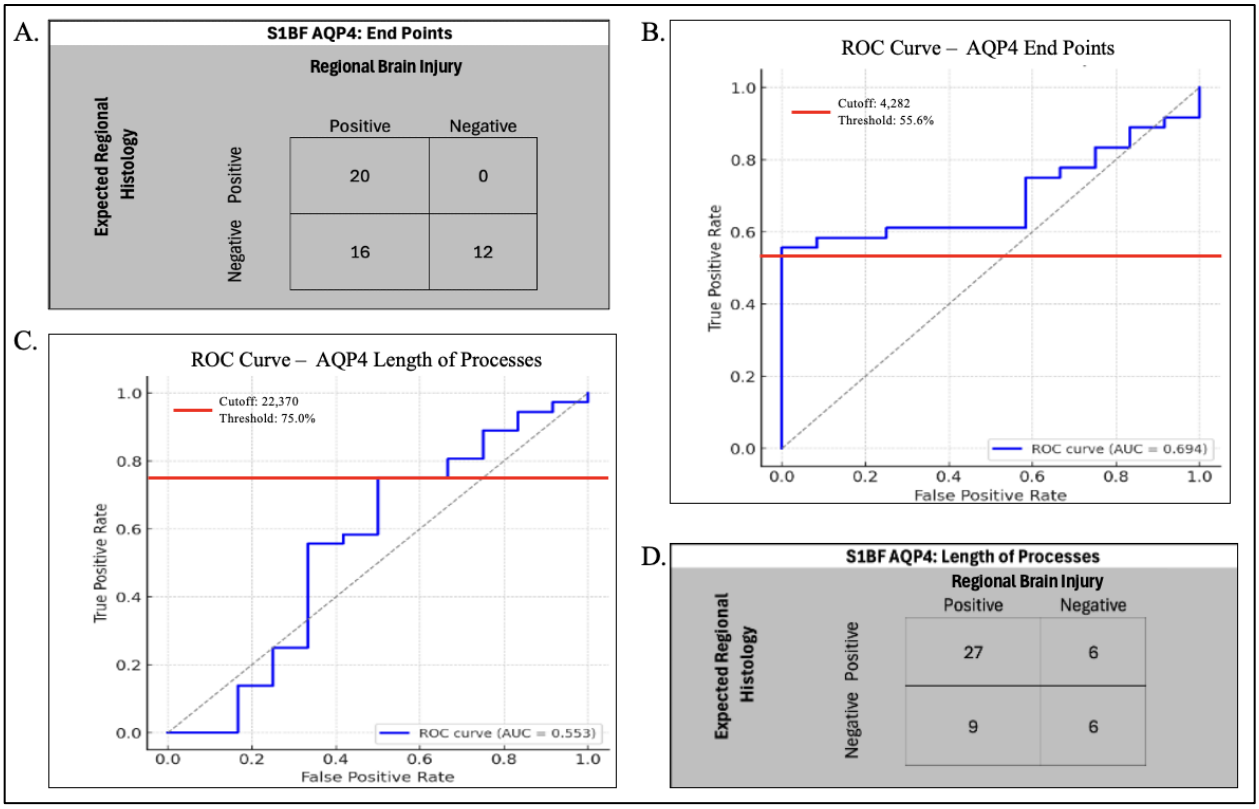

The AQP4 endpoints model produced an AUC = 0.694, indicating moderate discriminatory performance. The optimal cutoff, determined by Youden's Index, was 4,282 endpoints, producing the following confusion matrix: TN = 12, FP = 0, FN = 16, TP = 20. At this threshold, the model achieved a sensitivity of 55.6%, specificity of 100%, and overall accuracy of 66.7%. These results suggest that while the model is highly specific and avoids false positives,

its sensitivity is limited, indicating that endpoints alone may miss a substantial portion of positive cases and should ideally be combined with additional predictors for improved detection.

The AQP4 length of processes model produced an AUC of 0.553, indicating only slightly better-than-chance discrimination. The optimal threshold, determined using Youden's Index, was 22,369.78 length of processes, resulting in a confusion matrix of TN = 6, FP = 6, FN = 9, and TP =27. This corresponds to a sensitivity of 75.0%, specificity of 50.0%, and overall accuracy of 68.8%. While the length of processes showed modest ability to identify positive cases, the low specificity and marginal AUC suggest it is a weak standalone predictor and would likely require integration with additional variables to improve classification performance.

Figure 9.

ROC analysis and confusion matrices for MAP2 as a predictor of injury classification. (A) Confusion matrix for MAP2 endpoints with true positives (TP) = 6, false negatives (FN) = 30, false positives (FP) = 0, and true negatives (TN) = 12. (B) ROC curve for MAP2 endpoints with an area under the curve (AUC) of 0.451. Red horizontal line indicates the optimal classification threshold at sensitivity = 16.7%. (C) ROC curve for MAP2 length of processes with an AUC of 0.634. Red horizontal line indicates the optimal classification threshold at sensitivity = 83.3%. (D) Confusion matrix for MAP2 length of processes with true positives (TP) = 30, false negatives (FN) = 6, false positives (FP) = 7, and true negatives (TN) = 5.

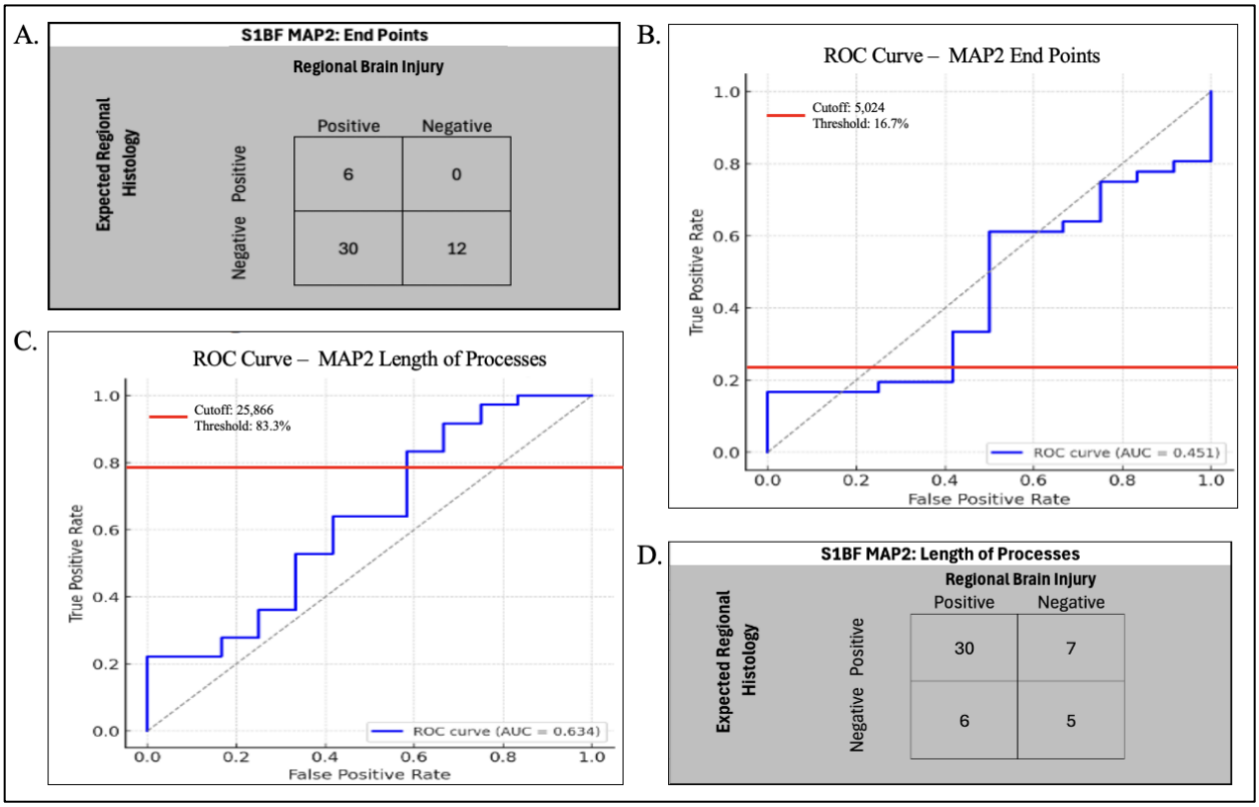

The MAP2 endpoints model produced an AUC = 0.451, indicating worse-than-chance discrimination. The optimal cutoff, identified using Youden's Index, was 5,024 endpoints, resulting in: TN = 12, FP = 0, FN = 30, TP = 6. At this threshold, the model achieved sensitivity of 16.7%, specificity of 100%, and overall accuracy of 37.5%. While the model perfectly avoided false positives, the very low sensitivity indicates that endpoints alone were unable to reliably detect most positive cases.

The MAP2 length of processes model produced an AUC = 0.634, indicating moderate discriminatory ability. The optimal cutoff was 25,866.18 length of processes, resulting in: TN = 5, FP = 7, FN = 6, TP = 30. At this threshold, the model achieved sensitivity of 83.3%, specificity of 41.7%, and overall accuracy of 72.9%. While the length of processes demonstrated a stronger ability to detect positive cases, the low specificity suggests a tendency toward false positives, and performance would likely improve if combined with additional predictive features.

Figure 10.

ROC analysis and confusion matrices for CD83 as a predictor of injury classification. (A) Confusion matrix for CD83 endpoints with true positives (TP) = 20, false negatives (FN) = 16, false positives (FP) = 1, and true negatives (TN) = 11. (B) ROC curve for CD83 endpoints with an area under the curve (AUC) of 0.750. Red horizontal line indicates the optimal classification threshold at sensitivity = 55.6%. (C) ROC curve for CD83 length of processes with an AUC of 0.491. Red horizontal line indicates the optimal classification threshold at sensitivity = 91.7%. (D) Confusion matrix for CD83 length of processes with true positives (TP) = 33, false negatives (FN) = 3, false positives (FP) = 9, and true negatives (TN) = 3.

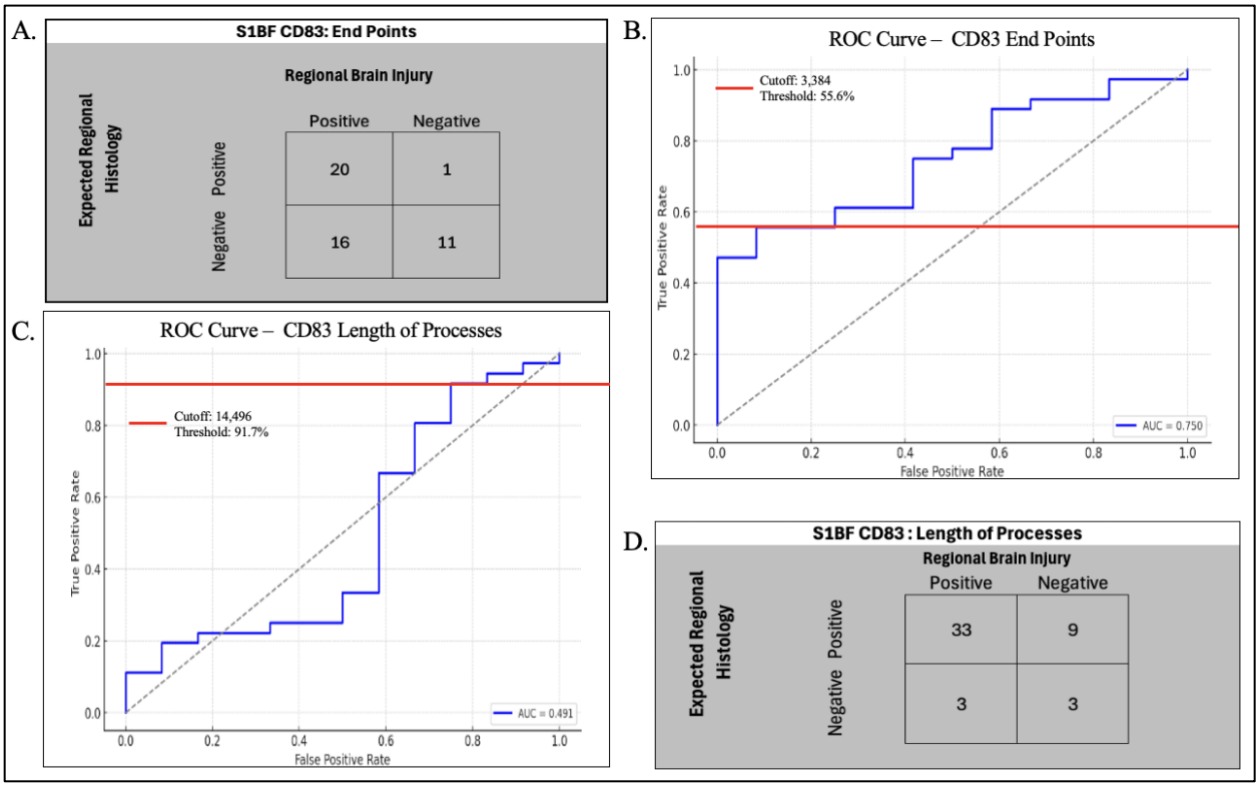

The CD83 endpoints model achieved an AUC = 0.750, indicating good discriminatory performance. The optimal cutoff, determined by Youden's Index, was 3,384 endpoints, producing the following confusion matrix: TN = 11, FP = 1, FN = 16, TP = 20. At this threshold, the model achieved a sensitivity of 55.6%, specificity of 91.7%, and an overall accuracy of 64.6%. These results indicate that the endpoints model is strong in correctly identifying negative cases (high specificity) but has moderate sensitivity, potentially missing some positive cases.

The CD83 length of processes model yielded an AUC = 0.491, suggesting no better-than-chance discrimination. The optimal cutoff was 14,496.33 length of processes, resulting in TN = 3, FP = 9, FN = 3, TP = 33. This corresponds to a sensitivity of 91.7%, specificity of 25.0%, and overall accuracy of 75.0%. While this model is highly sensitive and rarely misses positive cases, the low specificity means it misclassifies many non-injured cases as injured.

Figure 11.

ROC analysis and confusion matrices for GFAP as a predictor of injury classification. (A) Confusion matrix for GFAP endpoints with true positives (TP) = 6, false negatives (FN) = 30, false positives (FP) = 1, and true negatives (TN) = 11. (B) ROC curve for GFAP endpoints with an area under the curve (AUC) of 0.416. Red horizontal line indicates the optimal classification threshold at sensitivity = 8.3%. (C) ROC curve for GFAP length of processes with an AUC of 0.366. Red horizontal line indicates the optimal classification threshold at sensitivity = 55.6%. (D) Confusion matrix for GFAP length of processes with true positives (TP) = 3, false negatives (FN) = 33, false positives (FP) = 0, and true negatives (TN) = 12.

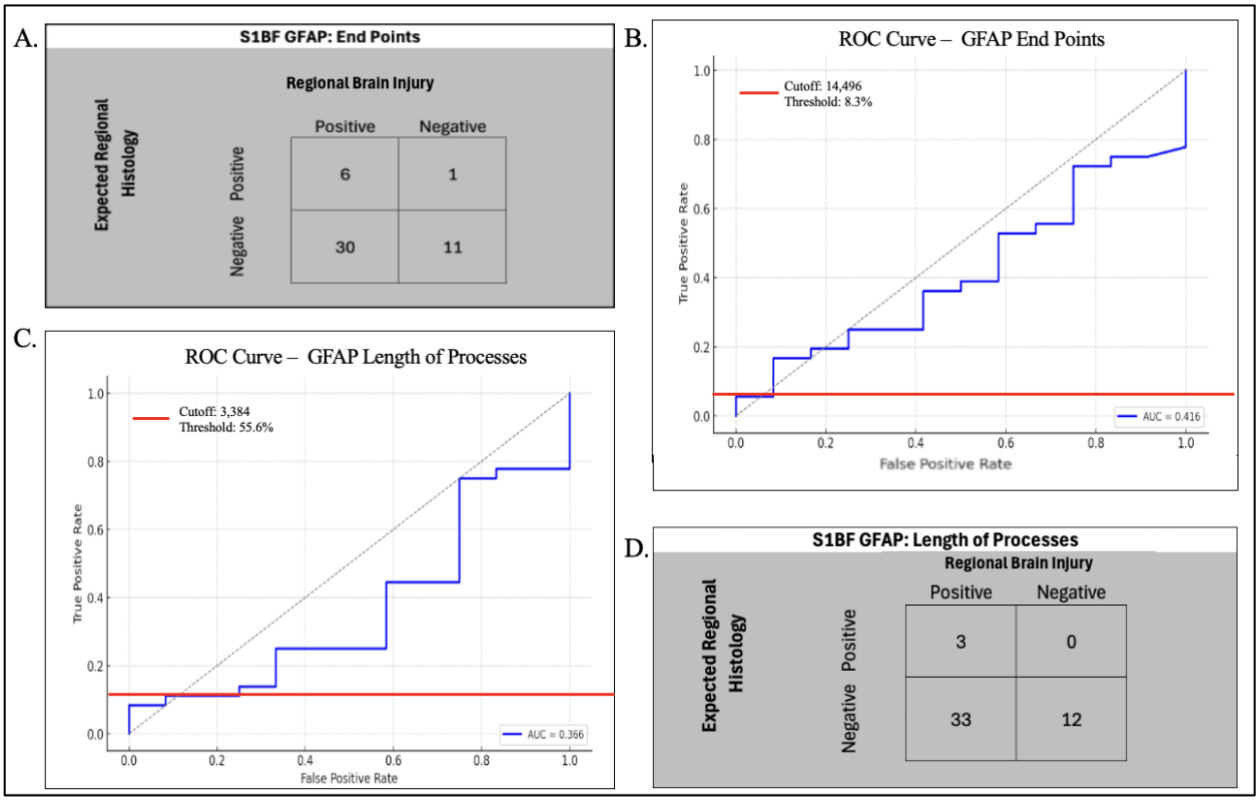

The GFAP endpoints model produced an AUC = 0.416, indicating poor discrimination. The optimal cutoff was 3,635 endpoints, producing: TN = 11, FP = 1, FN = 30, TP = 6. At this threshold, the model achieved sensitivity of 16.7%, specificity of 91.7%, and overall accuracy of 35.4%. These results indicate that the model is highly specific but detects few positive cases, limiting its usefulness as a standalone measure.

The GFAP length of processes model produced an AUC = 0.366, indicating very poor

discrimination and performance near chance. The optimal cutoff was 36,421.68 length of processes, producing: TN = 12, FP = 0, FN = 33, TP = 3. At this threshold, the model achieved sensitivity of 8.3%, specificity of 100%, and overall accuracy of 31.3%. While the model achieved perfect specificity, it detected very few true positives, further suggesting that the length of processes alone is not a reliable predictor for GFAP injury classification.

Figure 12.

ROC analysis and confusion matrices for Iba1+ as a predictor of injury classification. (A) Confusion matrix for Iba1+ endpoints with true positives (TP) = 0, false negatives (FN) = 36, false positives (FP) = 0, and true negatives (TN) = 12. (B) ROC curve for Iba1+ endpoints with an area under the curve (AUC) of 0.220. Red horizontal line indicates the optimal classification threshold at sensitivity = 0.0%. (C) ROC curve for Iba1+ length of processes with an AUC of 0.600. Red horizontal line indicates the optimal classification threshold at sensitivity = 41.7%. (D) Confusion matrix for Iba1+ length of processes with true positives (TP) = 15, false negatives (FN) = 21, false positives (FP) = 1, and true negatives (TN) = 11.

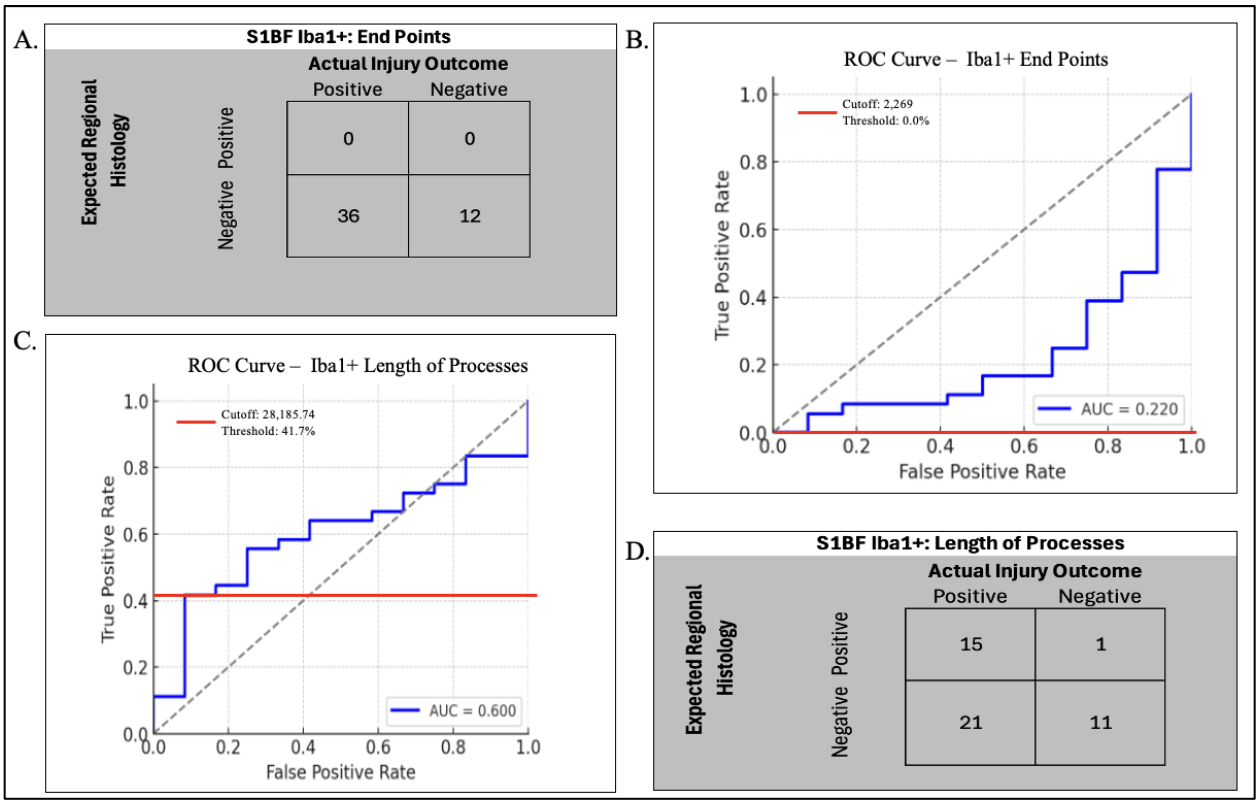

The Iba1+ endpoints model yielded an AUC of 0.220. The optimal threshold identified by Youden's Index was 2,269 endpoints, resulting in a confusion matrix of TP = 0, FP = 0, FN = 36, TN = 12. This corresponded to a sensitivity of 0.0%, specificity of 100%, and overall accuracy of 25.0%. While the model perfectly avoided false positives, it failed to detect any true positive cases.

The Iba1+ length of processes model produced an AUC of 0.600, representing only slightly better-than-chance discrimination. The optimal threshold, determined by Youden's Index, was 28,185.74 Branch Lengths, yielding a confusion matrix of TP = 15, FP = 1, FN = 21, TN = 11. This translated to a sensitivity of 41.7%, specificity of 91.7%, and overall accuracy of 54.2%. While the length of processes demonstrated better detection of positive cases compared to endpoints, the low sensitivity and marginal AUC suggest that it is a weak standalone predictor and would benefit from integration with additional variables to improve performance.

Qualitative Imaging-Pathologic Correspondence Analysis

To evaluate the correspondence between imaging signatures and actual injury status, qualitative confusion matrix analysis was performed comparing diffusion MRI hyperintensity patterns with histologically confirmed injury presence across brain regions. This analysis assessed the diagnostic performance of imaging in detecting injury-related pathophysiology by categorizing each region of interest as either imaging-positive or imaging-negative for hyperintensity, then comparing these classifications against the actual presence or absence of histologically confirmed injury markers.

The confusion matrix approach provides insight into the sensitivity and specificity of diffusion MRI signatures for detecting neuroinflammatory changes following experimental

diffuse TBI. Primary motor cortex (PMC) served as a control region where minimal injury-related changes were expected, while the S1BF represented the primary region of interest where robust injury pathophysiology has been consistently demonstrated. This comparative analysis enables assessment of both the regional specificity of imaging signatures and their diagnostic utility for detecting injury-induced pathological changes.**/**

Figure 14.

Confusion matrix for imaging performance in primary motor cortex (PMC). Matrix comparing diffusion MRI imaging classification (positive/negative for hyperintensity) against actual injury status in PMC regions (n = 8). True negatives (TN) = 8, false positives (FP) = 0, false negatives (FN) = 0, and true positives (TP) = 0.

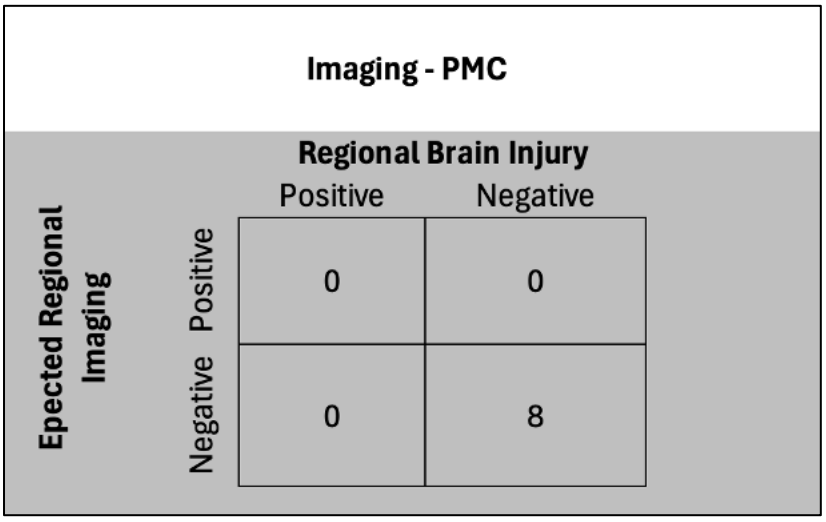

In the primary motor cortex (PMC) sham group, imaging findings were in complete agreement with actual injury status (n = 8; TP = 0, FN = 0, FP = 0, TN = 8). All sites were correctly classified as injury-negative, resulting in a specificity (true negative) and overall accuracy of 100.0%. Sensitivity, precision, and F1 score could not be calculated due to the absence of actual and predicted positives. The absence of any true or false positives is consistent with the sham condition, in which no injuries were present according to the actual injury

assessment. These results indicate that imaging reliably reflected the absence of injury in the PMC under sham conditions, as would be expected.

Figure 15.

Confusion matrix for imaging performance in primary somatosensory barrel field cortex (S1BF). Matrix comparing diffusion MRI imaging classification (positive/negative for hyperintensity) against actual injury status in S1BF regions (n = 8). True negatives (TN) = 2, false positives (FP) = 0, false negatives (FN) = 4, and true positives (TP) = 2.

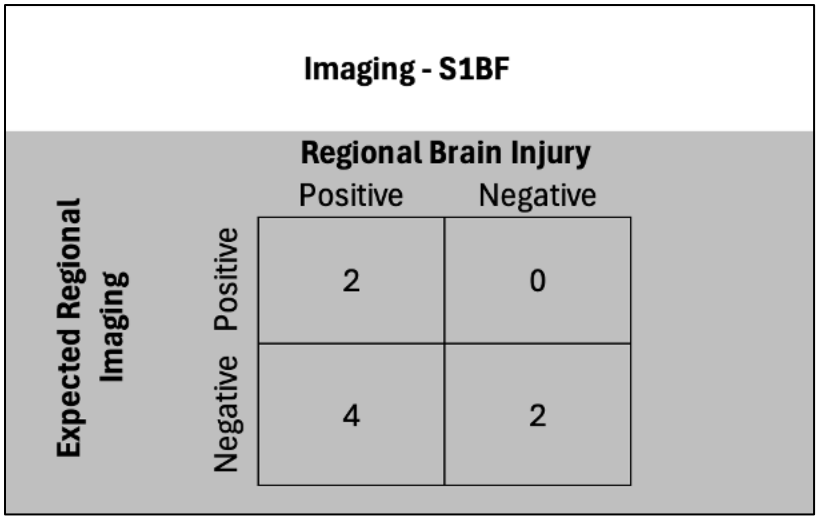

In the S1BF cortex, imaging showed limited agreement with the actual injury status (n = 8; TP = 2, FN = 4, FP = 0, TN = 2). Sensitivity (true positives) was 33.3%, specificity (true negatives) was 100.0%, precision was 100.0%, accuracy was 50.0%, and the F1 score was 50.0%. The two true positives represented sites where imaging correctly identified injury that was present. The two true negatives were sites without imaging-detectable abnormalities and no actual injury. No false positives occurred, indicating that imaging did not incorrectly classify any uninjured sites as injured. However, four false negatives were observed, representing sites with actual injury that were not detected on imaging, suggesting that some injury-related changes in the S1BF may fall below the detection threshold of the imaging modality. These findings

indicate that while imaging was highly specific in this region, its low sensitivity limited its ability to capture the full extent of injury.

Discussion

Aim 1: Verify a Radiologic-pathologic Correspondence between Activated Microglial Responses and Diffusion MRI

The present study successfully established a radiologic-pathologic correspondence between activated microglia and novel dMRI signatures in experimental diffuse TBI. Our findings demonstrate that regions of hyperintensity in both RTAP and RTOP maps correspond spatially with areas of dense microglial pathology, providing compelling evidence for the utility of advanced diffusion MRI techniques in detecting neuroinflammation following brain injury.

The selective sensitivity of dMRI metrics to activated microglia likely reflects several biophysical changes that occur during microglial activation. Activated microglia undergo characteristic morphological changes, including soma enlargement, process thickening, and increased cellular density within affected regions (Ziebell et al., 2015). These changes create physical barriers to water diffusion through multiple mechanisms: (1) increased cellular volume fraction reduces extracellular space, (2) enlarged cell bodies create more restricted diffusion compartments, and (3) retracted but thickened processes alter the directional organization of tissue microarchitecture (Guo et al., 2023; Yi et al., 2019).

The complementary information provided by RTAP and RTOP metrics suggests that microglial activation affects both overall tissue restriction (as measured by RTOP) and directional organization (as measured by RTAP). RTOP's sensitivity to overall cellular density changes aligns with the known accumulation of activated microglia in areas of pathology. In

contrast, RTAP's detection of directional changes may reflect the altered tissue architecture created by microglial morphological changes and their interaction with damaged neuronal processes.

The relative insensitivity of dMRI to other histopathologic markers of diffuse TBI (GFAP, MAP2, AQP4) at 7 DPI suggests that the technique may be particularly suited for detecting microglial-specific pathology (Iba1+, CD83) during the subacute injury phase. This specificity could represent a significant advantage over other neuroinflammation imaging approaches, such as PET imaging with radiolabeled ligands, which detect general microglial activation but cannot distinguish between different microglial morphologies or provide information about co-occurring astrocytic or neuronal changes.

The quantitative analysis of Iba1+ revealed significant regional differences in microglial morphology between the S1BF and motor cortex regions. In dense pathology regions, both microglial endpoints and LOP were significantly elevated in the S1BF compared to the motor cortex across both hemispheres. These findings are consistent with previous reports demonstrating preferential accumulation of pathology in the S1BF in experimental diffuse TBI models (Ziebell et al., 2012; Witcher et al., 2018).

The pattern of increased LOP without proportional increases in endpoints in non-dense regions suggests a complex activation response where microglia extend their territorial coverage without necessarily increasing branching complexity. This finding aligns with recent understanding of microglial activation as a spectrum rather than a binary state (Hammond et al., 2019) and may show where remaining microglia extend processes to cover the territory of damaged or lost neighboring cells.

The qualitative assessment between microglia and dMRI metrics revealed a striking spatial correspondence between dMRI hyperintensity and dense microglial pathology. Importantly, this correspondence demonstrated both sensitivity and specificity - hyperintensity was observed only in regions with dense pathology. These findings establish that dMRI metrics, specifically RTAP and RTOP, serve as sensitive indicators of dense microglial pathology, providing spatial information that directly corresponds to histologically confirmed neuroinflammation. However, the spatial resolution of dMRI limits discrimination between varying degrees of microglial density, while histological analysis can resolve individual cellular distributions. This selective correspondence suggests that dMRI signatures reflect specific experimental TBI-induced neuroinflammatory processes rather than non-specific tissue changes.

Aim 2: Explore additional radiologic-pathologic Correspondence among Histopathologic Targets of Diffuse TBI and dMRI Metrics through Immunohistochemistry

The analysis of additional histopathologic markers of diffuse TBI revealed variable regional differences between S1BF and motor cortex regions, with marker-specific patterns that provide insights into the biological basis of dMRI signatures.

CD83 demonstrated significant regional differences in the left hemisphere for both endpoints ($p = 0.03$) and length of processes ($p = 0.01$), with higher values in S1BF compared to the motor cortex. In the right hemisphere, only the length of processes showed significance ($p = 0.04$), while endpoints approached but did not reach significance ($p = 0.14$). Unlike the dense/non-dense regional patterns observed with Iba1+ staining, CD83 analysis was conducted as a general S1BF-to-motor cortex comparison, limiting direct assessment of whether CD83 follows the same heterogeneous distribution patterns as other microglial markers.

AQP4 showed hemispheric asymmetry in its regional distribution. In the right hemisphere, the length of processes was significantly higher in S1BF compared to the motor cortex ($p = 0.04$), while endpoints approached significance ($p = 0.09$). However, the left hemisphere showed no significant differences for either metric (endpoints $p = 0.30$, length of processes $p = 0.07$). This asymmetric pattern suggests that alterations in astrocytic water channel expression may contribute differently to pathophysiology between hemispheres, potentially reflecting the heterogeneous injury patterns characteristic of diffuse TBI.

GFAP demonstrated inconsistent regional patterns across hemispheres. The left hemisphere showed no significant differences between S1BF and motor cortex for either endpoints ($p = 0.23$) or length of processes ($p = 0.48$). Conversely, the right hemisphere showed a significant difference in endpoints ($p = 0.001$), but with motor cortex values actually higher than S1BF values, contrary to the expected pattern if astrocytic activation were driving dMRI signatures. Length of processes showed no significant difference in the right hemisphere ($p = 0.15$).

MAP2 showed minimal regional differences across both hemispheres. Neither endpoints nor length of processes differed significantly between S1BF and motor cortex in either hemisphere (all p-values > 0.25), suggesting that gross dendritic structural integrity remains relatively preserved at 7 days post-injury in both regions.

The variable results across different neuroinflammatory markers indicate that dMRI signatures do not uniformly correspond to all aspects of the neuroinflammatory response. The strongest and most consistent regional differences were observed with microglial markers (Iba1+ and CD83), while astrocytic and neuronal markers showed either absent, inconsistent, or contrary patterns. These findings suggest that at 7 days post-injury, dMRI hyperintensity in the

S1BF may be more closely associated with microglial activation than with other neuroinflammatory cellular responses.

The hemispheric asymmetries observed, particularly for AQP4 and GFAP, may reflect the heterogeneous nature of diffuse TBI pathophysiology, where injury-induced changes do not necessarily manifest uniformly across brain regions or hemispheres. The absence of visual pathological patterns for these markers, unlike the distinct clustering observed with microglial activation, necessitated the quantitative regional comparison approach and may explain why correspondence with dMRI signatures is less apparent than with microglial markers.

The 7-day post-injury timepoint may not capture peak responses for all neuroinflammatory markers. Previous studies have shown that microglial activation peaks around 3-7 days post-injury, while astrocytic responses may be more prolonged, potentially peaking at later timepoints (Ziebell et al., 2015; Burda et al., 2016). The timing of our analysis may therefore favor detection of microglial rather than astrocytic contributions to the dMRI signatures.

Diagnostic Performance of Histopathologic Markers and Imaging Signatures

The diagnostic performance analysis revealed significant variability across both histopathologic markers and imaging modalities, providing important insights into their potential use as biomarkers for diffuse TBI detection.

CD83 endpoints demonstrated the strongest discriminatory performance among cellular markers (AUC = 0.750), achieving a good sensitivity-specificity balance with high specificity (91.7%) and moderate sensitivity (55.6%). This finding supports CD83 as a reliable marker for

identifying activated microglia in experimental TBI, consistent with our pathological assessment showing significant differences between S1BF and motor cortex.

Both GFAP metrics performed poorly (AUC = 0.416 for endpoints, 0.366 for length of processes), with extremely low sensitivity (16.7% and 8.3%, respectively) despite high specificity. AQP4 showed mixed performance, with endpoints demonstrating moderate discriminatory ability (AUC = 0.694) and reasonable sensitivity (55.6%), while the length of processes showed only marginal performance (AUC = 0.553). These results align with our finding that astrocytic markers showed minimal or inconsistent regional differences between S1BF and motor cortex, suggesting that astrocytic activation may not be a prominent feature at 7 days post-injury or may require different analytical approaches for detection.

MAP2 demonstrated contrasting performance between metrics, with endpoints showing worse-than-chance discrimination (AUC = 0.451) and very low sensitivity (16.7%), while the length of processes achieved moderate performance (AUC = 0.634) with high sensitivity (83.3%) but poor specificity (41.7%). The poor performance of MAP2 endpoints suggests that dendritic branching complexity may not be significantly altered at 7 days post-injury, while the moderate performance of process length may reflect subtle changes in dendritic architecture that require further investigation.

The Iba1+ endpoints analysis revealed an unexpected but biologically meaningful pattern that initially appeared counterintuitive. The original ROC analysis yielded an AUC of 0.220, suggesting poor discriminatory performance. However, closer examination of the underlying morphological data revealed that injured brain regions consistently showed lower endpoint values (mean = 1,732) compared to uninjured regions (mean = 2,081), indicating a systematic inverse relationship.

This inverse pattern reflects the biology of microglial activation following TBI. In healthy brain tissue, ramified microglia maintain highly branched morphologies with numerous process endpoints extending radially from small cell bodies to survey the extracellular environment (Nimmerjahn et al., 2005). Following injury, these surveillance microglia undergo characteristic morphological changes, including process retraction and thickening, soma enlargement, and reduction in branching complexity (Ziebell et al., 2015). The reduction in endpoints observed in injured regions directly corresponds to this well-established activation phenotype, where microglia sacrifice morphological complexity for enhanced mobility and effector functions.

When the Iba1+ endpoints model was interpreted with inverted classification criteria (recognizing lower endpoint values as indicative of injury), the diagnostic performance improved dramatically to an AUC of 0.816, demonstrating strong discriminatory ability. At the optimal threshold of 1,939 endpoints, the inverted model achieved 78.8% sensitivity, 75.0% specificity, and 78.3% overall accuracy. This performance transformation underscores the importance of understanding the biological context underlying quantitative morphological metrics.

The complementary findings with Iba1+ length of processes (AUC = 0.600) support this interpretation. The moderate positive correlation between process length and injury status likely reflects the accumulation of activated microglia with shortened but potentially more numerous processes in injured regions, combined with the presence of rod microglia whose elongated morphology contributes to overall process length measurements. This dual pattern - reduced branching complexity alongside maintained or increased total process length - is consistent with the heterogeneous microglial response observed in diffuse TBI, where different activation states coexist within the same cortical region.

These findings highlight a critical consideration for biomarker development: the directionality of morphological changes must align with known pathophysiological processes. The initially "poor" performance of Iba1+ endpoints actually provides strong validation of the skeleton analysis methodology's ability to capture biologically relevant microglial activation signatures. This relationship may represent a more sensitive indicator of microglial activation than traditional markers, as it directly quantifies the loss of surveillance morphology that defines the transition from ramified to activated states.

For the imaging signatures, dMRI demonstrated different performance characteristics depending on the brain region examined. In the primary motor cortex, imaging had a perfect correspondence with injury status (100% specificity and accuracy), correctly identifying all regions as injury negative. This excellent performance in control regions validates the regional specificity of diffusion MRI signatures and confirms that hyperintensity patterns are not artifacts of the imaging process.

However, in the S1BF, imaging showed more complex performance characteristics with 100% specificity but only 33.3% sensitivity, resulting in 50% overall accuracy. While imaging never incorrectly classified uninjured regions as injured (no false positives), it failed to detect injury in 4/6 injured sites (false negatives). This pattern suggests that while diffusion MRI signatures are highly specific when present, they may not capture the full spectrum of injury-related pathophysiology in the S1BF region.

The variable performance across histopathologic markers emphasizes the complexity of injury classification using single morphological parameters. The generally high specificity but low sensitivity observed across most markers suggests that while these measures rarely misclassify uninjured tissue, they may miss subtle injury-related changes. This pattern suggests

that combining multiple markers or imaging parameters may be necessary for comprehensive injury detection. Additionally, the temporal specificity of our analysis (7 days post-injury) may contribute to the observed performance patterns. Different cellular responses peak at varying timepoints following injury, potentially explaining why some markers showed limited discriminatory ability while others, particularly microglial markers, demonstrated better performance. Future studies incorporating multiple timepoints could provide insights into optimal windows for biomarker detection and improve overall diagnostic accuracy.

Conclusion

The establishment of radiologic-pathologic correspondence between dMRI signatures and microglial activation represents a significant step toward developing clinically relevant biomarkers for diffuse TBI. The ability to non-invasively detect and quantify neuroinflammation could transform clinical practice by enabling earlier diagnosis, more accurate prognosis, and better monitoring of therapeutic interventions.

The regional specificity observed in our findings suggests that dMRI could potentially identify vulnerable brain regions or track the spatial evolution of injury pathophysiology over time. This capability could be particularly valuable for understanding individual differences in injury response and recovery patterns, supporting the development of personalized treatment approaches.

The comprehensive ROC analysis revealed important insights into the diagnostic utility of different histopathological markers. CD83 endpoints emerged as the most reliable cellular biomarker (AUC = 0.750), while the unexpected inverse relationship observed with Iba1+ endpoints (AUC = 0.816 when properly interpreted) demonstrates that microglial activation

signatures can be captured through reduced morphological complexity rather than traditional activation markers. This finding emphasizes the importance of understanding the biological context underlying quantitative morphological metrics for effective biomarker development.

However, several limitations must be addressed before clinical translation can occur. The *ex vivo* nature of our imaging limits direct clinical applicability, and validation through *in vivo* studies is necessary. Future studies should explore working with live animal models to represent patients suffering from TBI in a clinical setting effectively. Additionally, the temporal dynamics of the radiologic-pathologic correspondence require further investigation to determine optimal imaging windows for clinical assessment, as well as observation of different histopathologic markers of neuroinflammation, since they might peak at different time points. Longitudinal studies tracking the evolution of both imaging signatures and histopathological changes would provide valuable insights into the temporal relationships between neuroinflammation and diffusion alterations.

This study provides a comprehensive demonstration of radiologic-pathologic correspondence between advanced diffusion MRI metrics and neuroinflammatory processes in experimental diffuse TBI. Our findings establish that dMRI signatures, particularly RTAP and RTOP, serve as sensitive and specific indicators of microglial activation, with the strongest correspondence to dense microglial pathology.

The diagnostic performance analysis further validates the specificity of microglial markers over astrocytic and neuronal markers at this timepoint, with CD83 and properly interpreted Iba1+ endpoints showing strong discriminatory ability. The regional specificity and pathological selectivity of these signatures support their potential development as non-invasive biomarkers for neuroinflammation following brain injury. While additional neuroinflammatory

markers showed more complex relationships with imaging signatures, the robust correspondence with microglial activation provides a solid foundation for clinical translation and therapeutic monitoring applications.

References

Aguzzi, A., Barres, B. A., & Bennett, M. L. (2013). Microglia: Scapegoat, saboteur, or something else? *Science*, 339(6116), 156-161.

Avram, A. V., Sarlls, J. E., Barnett, A. S., Özarslan, E., Thomas, C., Irfanoglu, M. O., ... & Basser, P. J. (2016). Clinical feasibility of using mean apparent propagator (MAP) MRI to characterize brain tissue microstructure. *NeuroImage*, 127, 422-434.

Bachstetter, A. D., et al. (2015). Disease-related microglia heterogeneity in the hippocampus of Alzheimer's disease, dementia with Lewy bodies, and hippocampal sclerosis of aging. *Acta Neuropathologica Communications*, 3, 32.

Dixon, C.E., et al. (1987). A fluid percussion model of experimental brain injury in the rat. *Journal of Neurosurgery*, 67(1), 110-119.

Fick, R. H., Wassermann, D., Caruyer, E., & Deriche, R. (2016). MAPL: Tissue microstructure estimation using Laplacian-regularized MAP-MRI and its application to HCP data. *NeuroImage*, 134, 365-385.

Ginsberg, M.D., et al. (1997). Widespread metabolic depression and reduced somatosensory circuit activation following traumatic brain injury in rats. *Journal of Cerebral Blood Flow & Metabolism*, 17(11), 1193-1205.

Giordano, K. R., Denman, C. R., Dubisch, P. S., Akhter, M., & Lifshitz, J. (2021). An update on the rod microglia variant in experimental and clinical brain injury and disease. *Brain Communications*, 3(1), fcaa227.

Giordano, K. R. (2023). Precision identification and targeting of rod microglia in diffuse brain-injured cortex [Unpublished doctoral dissertation]. University of Arizona.

Guo, A. C., MacKay, A. L., Winters, K. V., Yang, J. A., Vavasour, I. M., Rauscher, A., ... & Li, D. K. (2023). Mapping microglia and astrocyte activation in vivo using diffusion MRI. *Science Advances*, 9(19), eabq2923.

Hall, K.D., et al. (2008). Neurodegeneration in the somatosensory cortex after experimental diffuse brain injury. *Neuroscience*, 151(2), 529-539.

Hammond, T. R., Dufort, C., Dissing-Olesen, L., Giera, S., Young, A., Wysoker, A., ... & Stevens, B. (2019). Single-cell RNA sequencing of microglia throughout the mouse lifespan and in the injured brain reveals complex cell-state changes. *Immunity*, 50(1), 253-271.e6.

Hutchinson, E. B., Schwerin, S. C., Avram, A. V., Juliano, S. L., & Pierpaoli, C. (2018). Diffusion MRI and the detection of alterations following traumatic brain injury. *Journal of Neuroscience Research*, *96*(4), 612-625.

Irfanoglu, M. O., Nayak, A., Jenkins, J., Hutchinson, E. B., Sadeghi, N., Thomas, C. P., & Pierpaoli, C. (2016). DR-TAMAS: Diffeomorphic registration for tensor accurate alignment of anatomical structures. *NeuroImage*, 132, 439-454.

Irfanoglu, M. O., Walker, L., Sarlls, J., Marenco, S., & Pierpaoli, C. (2012). Effects of image distortions originating from susceptibility variations and concomitant fields on diffusion MRI tractography results. *NeuroImage*, 61(1), 275-288.

Keren-Shaul, H., Spinrad, A., Weiner, A., Matcovitch-Natan, O., Dvir-Szternfeld, R., Ulland, T. K., ... & Amit, I. (2017). A unique microglia type associated with restricting development of Alzheimer's disease. *Cell*, 169(7), 1276-1290.e17.

Lee, H., Wintermark, M., Gean, A. D., Ghajar, J., Manley, G. T., & Mukherjee, P. (2008). Focal lesions in acute mild traumatic brain injury and neurocognitive outcome: CT versus 3T MRI. *Journal of Neurotrauma*, 25(9), 1049-1056.

Le, H., Zeng, W., Zhang, H., Li, J., Wu, X., Xie, M., ... & Shen, J. (2020). Mean apparent propagator MRI is better than conventional diffusion tensor imaging for the evaluation of Parkinson's disease: A prospective pilot study. *Frontiers in Aging Neuroscience*, 12, 563595.

Lifshitz, J., et al. (2009). Neurodegeneration in the somatosensory cortex after experimental diffuse brain injury. *Neuroscience*, 151(2), 529-539. Witcher, K.G., et al. (2018). Traumatic brain injury-induced neuronal damage in the somatosensory cortex causes formation of rod-shaped microglia. *Glia*, 66(12), 2719-2736.

Lifshitz, J., Rowe, R. K., Griffiths, D. R., Evilsizor, M. N., Thomas, T. C., Adelson, P. D., & McIntosh, T. K. (2016). Clinical relevance of midline fluid percussion brain injury: Acute deficits, chronic morbidities and the utility of biomarkers. *Brain Injury*, 30(11), 1293-1301.

Liu, Y. U., Ying, Y., Li, Y., Eyo, U. B., Chen, T., Zheng, J., ... & Wu, L. J. (2019). Neuronal network activity controls microglial process surveillance in awake mice via norepinephrine signaling. *Nature Neuroscience*, 22(11), 1771-1781.

Mathys, H., Adaikkan, C., Gao, F., Young, J. Z., Manet, E., Hemberg, M., ... & Tsai, L. H. (2017). Temporal tracking of microglia activation in neurodegeneration at single-cell resolution. *Cell Reports*, 21(2), 366-380.

Miller, G. F., DePadilla, L., & Xu, L. (2021). Costs of nonfatal traumatic brain injury in the United States, 2016. *Medical Care*, 59(5), 451-455.

Morrison, H. W., & Filosa, J. A. (2013). A quantitative spatiotemporal analysis of microglia morphology during ischemic stroke and reperfusion. *Journal of Neuroinflammation*, 10(1), 4.

Morrison, H. W., Young, K., Qureshi, M., Rowe, R. K., & Lifshitz, J. (2017). Quantitative microglia analyses reveal diverse morphologic responses in the rat cortex after diffuse brain injury. *Scientific Reports*, 7(1), 13211.

Nimmerjahn, A., Kirchhoff, F., & Helmchen, F. (2005). Resting microglial cells are highly dynamic surveillants of brain parenchyma in vivo. *Science*, 308(5726), 1314-1318.

Özarslan, E., Koay, C. G., Shepherd, T. M., Komlosh, M. E., İrfanoğlu, M. O., Pierpaoli, C., & Basser, P. J. (2013). Mean apparent propagator (MAP) MRI: A novel diffusion imaging method for mapping tissue microstructure. *NeuroImage*, 78, 16-32.

Pasternak, O., Sochen, N., Gur, Y., Intrator, N., & Assaf, Y. (2022). Free water elimination and mapping from diffusion MRI. *Magnetic Resonance in Medicine*, 62(3), 717-730.

Pierpaoli, C., Walker, L., Irfanoglu, M. O., Barnett, A., Basser, P., Chang, L. C., ... & Wu, M. (2010). TORTOISE: An integrated software package for processing of diffusion MRI data. In *ISMRM 18th annual meeting* (Vol. 1597).

Shemer, A., Erny, D., Jung, S., & Prinz, M. (2015). Microglia plasticity during health and disease: An immunological perspective. *Trends in Immunology*, 36(10), 614-624.

Taylor, C. A., Bell, J. M., Breiding, M. J., & Xu, L. (2017). Traumatic brain injury–related emergency department visits, hospitalizations, and deaths—United States, 2007 and 2013. *MMWR Surveillance Summaries*, 66(9), 1-16.

Tay, T. L., Sagar, J. D., Grün, D., & Prinz, M. (2018). Unique microglia recovery population revealed by single-cell RNAseq following neurodegeneration. *Acta Neuropathologica Communications*, 6(1), 87.

Taylor, S. E., Morganti-Kossmann, C., Lifshitz, J., & Ziebell, J. M. (2014). Rod microglia: A morphological definition. *PLoS One*, 9(5), e97096.

Tremblay, M. È., Stevens, B., Sierra, A., Wake, H., Bessis, A., & Nimmerjahn, A. (2011). The role of microglia in the healthy brain. *Journal of Neuroscience*, 31(45), 16064-16069.

Wake, H., Moorhouse, A. J., Jinno, S., Kohsaka, S., & Nabekura, J. (2009). Resting microglia directly monitor the functional state of synapses in vivo and determine the fate of ischemic terminals. *Journal of Neuroscience*, 29(13), 3974-3980.

Witcher, K. G., Bray, C. E., Dziabis, J. E., McKim, D. B., Benner, B. N., Rowe, R. K., ... & Godbout, J. P. (2018). Traumatic brain injury-induced neuronal damage in the somatosensory cortex causes formation of rod-shaped microglia that promote astrogliosis and persistent neuroinflammation. *Glia*, 66(12), 2719-2736.

Wolf, S. A., Boddeke, H. W., & Kettenmann, H. (2017). Microglia in physiology and disease. *Annual Review of Physiology*, 79, 619-643.

Yi, S. Y., Barnett, B. R., Torres-Velázquez, M., Zhang, Y., Hurley, S. A., Rowley, P. A., ... & Johnson, S. C. (2019). Detecting microglial density with quantitative multi-compartment diffusion MRI. *Frontiers in Neuroscience*, 13, 81.

Ziebell, J. M., Adelson, P. D., & Lifshitz, J. (2015). Microglia: Dismantling and rebuilding circuits after acute neurological injury. *Metabolic Brain Disease*, 30(2), 393-400.

Ziebell, J. M., Ray-Jones, H., & Lifshitz, J. (2017). Nogo presence is inversely associated with shifts in cortical microglial morphology following experimental diffuse brain injury. *Neuroscience*, 359, 209-223.

Ziebell, J. M., Taylor, S. E., Cao, T., Harrison, J. L., & Lifshitz, J. (2012). Rod microglia: Elongation, alignment, and coupling to form trains across the somatosensory cortex after experimental diffuse brain injury. *Journal of Neuroinflammation*, 9(1), 247.